Single cell RNA sequencing in isogenic *FUS* and *TARDBP* mutant ALS lines reveals early mitochondrial dysfunction as a common pathway in motor neurons

Christoph Schweingruber[1,2], Jik Nijssen[2], Jonas Mechtersheimer[3], Stefan Reber[3], Michaela Keuper[4], Irene Mei [1], Julio Aguila Benitez[2], Niamh O'Brien[3], Martin Jastroch[4], Marc-David Ruepp[3*], Eva Hedlund[1,2*]

[1] Department of Biochemistry and Biophysics, Stockholm University, Stockholm, Sweden.

[2] Department of Cell and Molecular Biology, Karolinska Institutet, Stockholm, Sweden.

[3] UK Dementia Research Institute Centre at King's College London, Institute of Psychiatry, Psychology and Neuroscience, King's College London, Maurice Wohl Clinical Neuroscience Institute, London, United Kingdom.

[4] Department of Molecular Biosciences, The Wenner-Gren Institute, Stockholm University, Stockholm, Sweden.

[*] equal contribution

Correspondence to: eva.hedlund@dbb.su.se and marc-david.ruepp@kcl.ac.uk

Abstract

Mutations in the RNA/DNA-binding proteins FUS and TDP-43 cause amyotrophic lateral sclerosis (ALS) with distinct neuropathological features. It is currently unclear how these gene mutations lead to selective motor neuron death and if there are common mechanisms across disease causations. Using single cell RNA sequencing of neurons derived from isogenic induced pluripotent stem cell lines, we demonstrate that motor neurons harbouring FUS P525L or FUS R495X mutations show a 4.9- to 15.5-fold larger transcriptional response than interneurons. About 20% of transcripts were coregulated across FUS mutations in motor neurons and about half of these were caused by FUS gain-of-function. Comparison with TDP-43 M337V motor neurons, identified common mitochondrial dysfunction across gene mutations. Metabolic assessment confirmed a decrease in mitochondrial respiration and ATP turnover in mutant *FUS* and *TARDBP* motor neurons and live cell microscopy revealed impaired mitochondrial motility across ALS motor axons. Thus, we have identified early

mitochondrial dysfunction in motor neurons shared across ALS-causative mutations, that could have major implications for their survival and which could be targeted therapeutically.

Main

Amyotrophic lateral sclerosis (ALS) is a devastating disease with no cure or effective treatments which is defined by the selective loss of corticospinal motor neurons and somatic motor neurons in the brain stem and spinal cord, that innervate skeletal muscles, with resulting spasticity, muscle atrophy and paralysis.[1–3] The majority of ALS cases appear sporadic with unknown etiology, but the disease can also be inherited and caused by mutations in e.g. superoxide dismutase 1 (SOD1), the DNA/RNA-binding proteins TDP-43 (encoded by the *TARDBP* gene) or FUS and C9orf72.[4–8] Irrespective of the disease causation, selective degeneration of somatic motor neurons is seen, which has been attributed to their high firing rate, long axons and hyperbranching with up to 2,000 muscle fibers and high energy demand and vulnerability to ER stress.[1,9,10] Mutations in *FUS* cause about 1-5% of familial ALS cases and are present in a number of sporadic ALS cases.[5,6,11] FUS is a nucleocytoplasmic shuttling DNA- and RNA-binding hnRNP (heterogeneous ribonucleoprotein) which partakes in a broad range of cellular functions. Most FUS-linked ALS mutations destroy the protein's nuclear localization signal, resulting in cytoplasmic mis-localization, accumulation and formation of large cytoplasmic inclusions that sequester many other proteins and RNA species in neurons and glial cells.[5,6,12] Several studies point to toxic gain-of-function (GOF) of FUS in the cytoplasm. Cytoplasmic expression of FUS in mice causes motor neuron degeneration while FUS knockout or wild-type FUS expressed at physiological level, and localized mainly to the nucleus, leave motor neurons unharmed.[13–15] FUS in the cytoplasm may drive phase transition and solidify FUS-containing RNA granules over time[14,16] or it may augment the cytosolic functions of FUS in mRNA stabilization, transport and local translation.[17] Mutations in *TARDBP*, cause ALS in 3% of familial and 2% of sporadic cases, in which TDP-43 is mis-localized from the nucleus to the cytoplasm of neurons and glial cells.[8,18–21] Misexpression or overexpression of wild-type or ALS-mutant *TARDBP* in mice results in neuronal toxicity and motor neurons loss in the absence of cytoplasmic inclusions, which indicates that cytoplasmic aggregation is not a prerequisite for a neurodegenerative phenotype.[22,23] Depletion of *TARDBP* from cells causes massive effects on RNA metabolism, as it maintains faithful gene

expression by repressing the splicing of non-conserved cryptic exons,[24] e.g. in *UNC13A* and *STMN2.*[25–27] TDP-43 mis-localization to the cytoplasm is seen in the majority (>95%) of all ALS patients,[28–30] and may indicate loss-of-function of TDP-43*,* expanding the relevance of RNA metabolism to most ALS cases. It is currently unclear how mutations in *FUS* and *TARDBP* lead to selective motor neuron death. We therefore aimed to unravel if there were any shared pathways that link these different genetic etiologies of ALS and if these uniquely affected motor neurons. Towards this purpose we used induced pluripotent stem cells (iPSCs), which can model disease phenotypes in ALS and intracellular dysfunctions, including protein aggregation and axonal transport defects.[31–33] Cross-comparison of patient-derived iPSC lines can be complicated by differences in genetic backgrounds, which may obscure subtle changes when several lines are compared across mutations. We therefore used isogenic CRISPR/Cas9 edited lines where each ALS-causative mutation was introduced onto the same control iPSC line. Here we report the single cell RNA sequencing across neuron types derived from isogenic lines harboring FUS P525L or R495X point mutations, knockout (KO) of *FUS* or the *TARDBP* M337V mutation followed by metabolic assessment. Collectively our findings reveal early mitochondrial dysfunctions exacerbated in motor neurons across *FUS* mutant lines that were related to a GOF and shared with the mutant *TARDBP* line in addition to being present in iPSC lines from individuals with *C9orf72*-linked ALS. The impairment in mitochondrial respiration and ATP turnover across several mutant *FUS* and *TARDBP* lines and the decrease in mitochondrial motility seen across ALS motor axons support a convergence of motor neuron intrinsic dysfunction and provide a foundation for therapeutically improving mitochondrial activity in ALS.

Results

Isogenic mutant ALS-FUS lines reveal early cell-type specific transcriptional dysregulation

To understand how *FUS*-ALS affects human motor neurons and interneurons differentially and discern GOF versus loss-of-function (LOF) mechanisms, we aimed to introduce aggressive mutations in human iPSCs and compare these lines to a *FUS* KO. To select *FUS* mutations for this purpose, we aggregated clinical features from 502 published ALS cases with *FUS* mutations in order to conduct a meta-analysis (Extended Data Fig. 1a). The results affirmed

that the FUS P525L mutation results in the earliest onset (at age of 21 ± 8 years, mean ± sd) followed by FUS R495X (at age of 31 ± 11 years) and both mutations progress rapidly to respiratory failure or death within 17 ± 10 and 20 ± 18 months, respectively (Extended Data Fig. 1b,c) and were selected for our studies. In contrast, most other *FUS* mutations lead to disease in midlife or later (age of 41 ± 18 years). CRISPR/Cas9-mediated genome editing was used to introduce a homozygous *FUS* R495X mutation into the DF6-9-9T.B control line (Extended Data Fig. 2a,b) and compared to a *FUS P525L* mutation (heterozygous or homozygous) [12] which were generated on the same background. Introduction of the mutations was confirmed by dye terminator sequencing following PCR amplification of the edited loci. We also used a *FUS* KO line which had been generated on the same background that employs a gene trap in the first intron of *FUS*[34] (Fig. 1a). The pluripotency of the generated iPSC lines was established by immunofluorescence microscopy using antibodies against POU5F1 (OCT-3/4) and NANOG (Extended Data Fig. 2c). Immunofluorescent staining against FUS in iPSCs confirmed the loss of FUS in the KO line, and the redistribution of FUS from nucleus to cytoplasm in the R495X and P525L lines. The homozygous lines showed a complete redistribution of FUS from nucleus to cytoplasm, while the heterozygous P525L line showed expression in both nucleus and cytoplasm, as expected (Extended Data Fig. 2d). To dissect the role of FUS' LOF and GOF in lower motor neuron vulnerability, isogenic iPSC lines were specified to spinal motor neurons and interneurons using two distinct protocols. The first protocol generates 30-40% of interneurons,[35] here termed the heterogeneous protocol (Extended Data Fig. 3a,f), while the second protocol generates 60-80% of motor neurons,[32,36,37] here termed the homogeneous protocol (Extended Data Fig. 3c,g). Differentiation of iPSC lines showed that motor neurons (ISL1/2$^+$) and interneurons were readily generated (Extended Data Fig. 3b,d) and that the proportions of specific neuronal populations and progenitors were consistent across lines, with no marked effect of the mutations on cell type specification (Extended Data Fig. 3f,g). Most ALS-associated *FUS* mutations result in a change in subcellular distribution and cytoplasmic accumulation of the mutant protein, which is thought to be toxic.[38] Therefore, we validated mutant FUS mis-localization in motor neurons derived from the genome edited lines by immunofluorescence, which showed cytoplasmic accumulation of FUS P525L in ISL1/2$^+$ neurons, unlike for the control line. The P525L motor neurons also retained some signal in the nucleus, similar to what has been seen for other *FUS* mutations that interfere with the nuclear localization

signal.[39,40] We also confirmed the ablation of FUS in the FUS KO motor neurons (Fig. 1b, Extended Data Fig. 4a). We used antibodies with specific epitopes spanning the FUS P525 position (wild-type P525P and mutant P525L) to delineate heteroallelic mutant and wild-type FUS in immunofluorescence staining (Extended Data Fig. 4b,d). The specificity of the antibodies was confirmed by western blots of whole cell lysates from iPSCs (Extended Data Fig. 4c). We found that in FUS P525L heterozygous motor neurons, wild-type FUS localized mainly to the nucleus, while mutant FUS P525L localized to both cytoplasm and nucleus. In homozygous FUS P525L and in FUS R495X motor neurons, we found a clear mis-localization of mutant FUS. Thus, we have generated isogenic iPSC lines in which FUS LOF and GOF in ALS can be studied across mutations and neuron types to reveal why motor neurons are particularly vulnerable and if there are common pathways that are dysregulated across mutations.

Following characterization of the isogenic FUS mutant and KO lines, we subjected differentiated cultures to FACS to isolate individual live cells and conducted Smart-seq2 single cell RNA sequencing (Fig. 1a). After quality control (see methods section), 1,415 cells remained, which were classified according to a decision tree into motor neurons, interneurons and neuronal progenitor cells (Extended Data Fig. 3e). Cells were plotted using UMAP (uniform manifold approximation and projection), which demonstrated clustering of motor neurons, interneurons and neuronal progenitors (Fig. 1c). Cells originating from the different isogenic lines distributed across all clusters (Fig. 1d) consistent with the observation that all lines generate neurons at similar proportions (Extended Data Fig. 3f,g). UMAP projection of neurons only, after removal of progenitors, showed a clear separation of motor neurons and interneurons with clustering of V2a interneurons across lines (Fig. 1e,f). V2a excitatory interneurons are also prone to degeneration in ALS as shown in SOD1^{G93A} mice[41] and appear more vulnerable than V1 inhibitory interneurons to early disease processes.[42] Thus, we separated these from other interneuron types in cross-comparisons with motor neurons to delineate potential gradients in vulnerability. General neuronal markers (*MAPT*, *NEFM*, *SNAP25*) were highly expressed across neuron types while markers of proliferating cells (*SOX2*, *MKI67*, *CDK1*) were absent (Fig. 1g). Motor neurons showed expression of *ISL1*, *ISL2*, *MNX1*, *UTS2*, *SLC18A3*, and *SLC5A7* (Fig. 1g), while the presence of glutamatergic markers combined with *SOX14* and *VSX2* (*Chx10*) demarked V2a interneurons (Fig. 1h). In

conclusion, we find that single cell RNA sequencing can readily identify motor neurons and interneuron subpopulations derived from the isogenic iPSC lines and that neither *FUS*-ALS mutations (heterozygous or homozygous) nor FUS KO impair the generation of these cell types. Thus, we proceeded to investigate if the *FUS* mutations and FUS KO affect neurons in a cell-type specific manner. First, we established that *FUS* mRNA remained at comparable levels with only small changes across cell types in the different cell lines. *FUS* mRNA was only slightly upregulated in FUS P525L homozygous motor neurons compared to control (Fig. 1i, Supplementary Table 1). We then performed differential gene expression analysis (DEA) in motor neurons, V2a interneurons and other interneurons between FUS mutations and the control line in our single cell data. In each cell line, we found that motor neurons displayed unique transcriptional changes associated with the individual mutation and little overlap with V2a and other interneurons, suggesting that the majority of transcriptional adaptation and dysregulation events are specific to motor neurons (Fig. 1j). Furthermore, motor neurons demonstrated much larger transcriptional responses to the *FUS* mutations and loss of FUS than the interneuron groups. V2a interneurons showed a surprisingly small response to the FUS mutations compared to the other, presumably more resilient, interneuron group. This analysis demonstrated that introducing the R495X or the P525L mutations resulted in a stronger transcriptional response than knocking out FUS. This is clearly indicative of both LOF and GOF being altered in mutant FUS lines. Furthermore, homozygous introduction of the FUS P525L mutation resulted in 2,365 DEGs unique to motor neurons, while the same heterozygous mutation induced 1,075 DEGs, showing a dose response to this gene mutation (Fig. 1j, Supplementary Table 2). The homozygous FUS R495X mutation induced 1,064 DEGs, which is less than half of that elicited by the more aggressive FUS P525L mutation, indicating that the transcriptional dysregulation is correlated to the severity of the mutation (Fig. 1j). In conclusion, our analysis demonstrates that each neuron type exhibits unique transcriptional responses to *FUS* mutations and FUS KO. It also shows that *FUS* mutations elicit the largest transcriptional response in motor neurons and that this appears correlated with the aggressiveness of the mutation, gene dosage as well as FUS mis-localization, and may underlie the cell-type specific vulnerabilities to *FUS*-ALS.

Single cell RNA sequencing points to shared gain-of-function pathways in motor neurons across FUS mutations

To clarify whether motor neuron-specific DEGs were unique to the individual *FUS* mutations or shared across lines and the FUS KO we interrogated the transcriptomes across the lines (Fig. 2a). We found 471 DEGs that were commonly altered among FUS R495X and the P525L heterozygous as well as homozygous lines, indicative of a shared transcriptional response. Of those, 116 DEGs were further shared with the FUS KO motor neurons and are thus associated with a LOF in *FUS*-ALS (Fig. 2b, red). Thus, 355 DEG were unique to mutant FUS motor neurons and can therefore be classified as *bona fide FUS*-ALS associated GOF changes (Fig. 2b, green). The pathways that are associated with these changes were assessed by gene set enrichment analyses (GSEA), leading to the identification of 655 biological processes changed in response to any of the investigated FUS mutations. Comparison of gene ontologies (GO) between the lines (Fig. 2c) identified 81 shared biological processes across mutant *FUS*-ALS motor neurons, eleven that were associated with a *FUS*-ALS LOF (Fig. 2c, red) and 70 that were not and thus represent *FUS*-ALS GOF (Fig. 2c, green). We found only nine biological processes that were unique to the FUS KO line and do not reflect changes found in the *FUS*-ALS motor neurons (Fig. 2d). Altogether, this comparative analysis suggests that the majority of *FUS*-ALS dysregulated processes are due to FUS GOF. The GO biological processes unique to LOF in *FUS*-ALS motor neurons included RNA splicing, establishment of RNA localization and nuclear export together with processes related to synapse organisation and activity, dendritic spine development and neuronal projections (Fig. 2e). The GO biological processes unique to *FUS*-ALS GOF included metabolic pathways e.g. downregulation of aerobic respiration, oxidative phosphorylation, and mitochondrial respiratory chain complex assembly, regulation of RNA metabolism e.g. upregulation of mRNA 3' end processing, regulation of RNA splicing, regulation of mRNA processing, RNA localization, and RNA export from nucleus and the upregulation of processes involved in organelle and vesicle turn-over e.g. endoplasmatic reticulum tubular network organization, establishment of organelle organization, and Golgi vesicle transport among others (Fig. 2f). We also employed commercially curated gene ontology sets to independently identify dysregulated pathways in our data. Using Qiagen's Ingenuity pathway analysis[43] with DEGs between mutant FUS and control motor neurons, we identified 59 pathways that were significantly altered in *FUS*-ALS motor neurons at a false

discovery rate (FDR) cut-off at < 0.1, and not at all in V2a interneurons and to a very low extent in the other interneurons (Fig. 2g, Supplementary Table 3). Among the top ten pathways identified in this analysis were mitochondrial dysfunction and oxidative phosphorylation, synaptogenesis signalling pathway, as well as pathways regulating translation and protein stability (EIF2 signalling, regulation of eIF4 and p70S6K signalling, mTOR signalling and protein ubiquitination pathway). Altogether our single cell transcriptome analysis in FUS motor neurons points to shared pathways that might underly *FUS*-ALS pathological mechanisms, most of which are associated with FUS GOF.

The ALS-causative TDP-43 M337V mutation leads to massive transcriptional dysregulation unique to motor neurons

Similar to FUS, TDP-43 is an RNA/DNA-binding protein and ALS-causative mutations in the *TARDBP* gene give rise to broad effects on RNA metabolism.[24,27,44,45] Furthermore, as TDP-43 inclusions represent a pathological hallmark of the majority (>95%) of ALS cases,[28–30] RNA dysregulation is implicated in ALS irrespective of causation.[46] We reasoned that an analysis of *TARDBP*-ALS may give clues to downstream disease mechanisms across ALS cases more broadly. We thus generated another isogenic iPSC line (on the DF6-9-9T.B control background) that harbored the ALS-causing *TARDBP* M337V mutation using CRISPR/Cas9-mediated genome editing (Fig. 3a). After verification of successful genome editing and that the mutation did not result in altered cellular TDP-43 protein levels in the iPSCs (Extended Data Fig. 5a-c), we conducted Smart-seq2 single cell RNA sequencing on motor neurons and interneurons (Fig. 3a) and combined it with our FUS data set. Following the same cell type classification (Extended Data Fig. 3e), we found that TDP-43 M337V cells from both protocols blended into our single cell dataset in UMAP projections (Fig. 3b,c). The localization of TDP-43 did not vary between control and TDP-43 M337V motor neurons, similar to mouse models of the mutation.[47,48] However, we observed a moderate increase in phosphorylated TDP-43 foci in the cytoplasm (Fig. 3d). DEA with DESeq2 demonstrated that the *TARDBP* M337V mutation induced a massive transcriptional response in motor neurons with 2,284 DEGs, of which 2,143 were unique to motor neurons and the majority upregulated compared to the isogenic control. V2a and the other interneuron population on the other hand, showed only moderate responses with 145 DEGs for V2a and 196 DEGs for other interneurons, of which a

minority (17 DEGs) were shared between the two interneuron groups (Fig. 3e). The level of *TARDBP* mRNA remained stable across cell types and lines (Fig. 3f, Supplementary Table 1) and thus does not explain the huge difference in cell-type specific transcriptional regulation with the ALS-causative mutation. Collectively, we find that the *TARDBP* M337V mutation mainly triggered a response in motor neurons similarly to *FUS* mutations, while interneurons remained rather unaffected in their gene expression patterns.

Transcriptional changes shared across ALS-causative mutations in *FUS*, *TARDBP* and *C9orf72* implicate mitochondrial dysfunction within motor neurons

Disease histopathology appears unique with *FUS*[5,6] and *TARDBP*[18,49] mutations, but the selective motor neuron degeneration, glial activation and clinical presentation is similar, suggesting a convergence of pathomechanisms.[50] We reasoned that the comparison across *FUS* and *TARDBP* gene mutations could reveal if there are intrinsic pathways and DEGs central to motor neurons irrespective of the composition of aggregated proteins and disease etiology (Fig. 4a). We identified 1,088 DEGs that were uniquely regulated in TDP-43 M337V but not in the FUS motor neurons (Fig. 4b, Supplementary Table 2). There was considerable overlap between DEGs in TDP-43 M337V and FUS P525L homozygous motor neurons, with 578 DEGs shared uniquely between the two lines (Fig. 4b, blue). Furthermore, TDP-43 M337V motor neurons shared 160 DEGs with *FUS*-ALS GOF (Fig. 4b, yellow) and 64 DEGs with *FUS*-ALS LOF (Fig. 4b, red). The GSEA between the TDP-43 M337V and control motor neurons revealed 423 biological processes that were altered in the mutant motor neurons (Fig. 4c, Supplementary Table 3). Comparing mutant TDP-43 M337V dysregulated processes with those found in *FUS* motor neurons (Fig. 2c-g) shows that the majority (370 biological processes) are unique to the *TARDBP* mutation (Fig. 4c). e.g. regulation of cholesterol biosynthetic process, ribonucleotide complex biogenesis, negative regulation of cellular amide metabolic process and ncRNA export from nucleus (Extended Data Fig. 5d). However, the majority of FUS dysregulated processes were also affected in TDP-43 M337V motor neurons, with eight out of 11 FUS LOF processes and 44 out of 69 FUS GOF overlapping with GO terms in the mutant TARDBP motor neurons (Fig. 4c). This indicates that there is shared transcriptional dysregulation across the isogenic ALS lines that relate to early and common dysfunctions in motor neurons. Upon closer inspection, we find that the biological processes

that were shared across mutant *TARDBP* and *FUS* LOF mostly relate to RNA metabolism (RNA splicing, mRNA processing, establishment of RNA localization), nuclear export and neuronal specific functions (dendritic spine development and neuron projection organization). The biological processes that were shared between mutant *TARDBP* and *FUS* GOF were upregulation of a number of RNA metabolic processes, e.g. RNA 3' end processing, regulation of splicing, RNA localization, RNA export from nucleus, mRNA transport as well as downregulation of energy metabolic processes, e.g. oxidative phosphorylation and aerobic respiration (Fig. 4d).

By comparing the motor neuron response across *FUS* and *TARDBP* mutations, we identified a shared and intrinsic signature of potentially early cellular dysfunction across ALS-causative mutations, which is characterized by changes in RNA metabolism, neuronal organization and mitochondrial energy metabolism and may explain their particularly susceptibility in ALS. To investigate if our findings were relevant more broadly across ALS, we compared our dataset with published bulk RNA sequencing from iPSC-derived cultures containing mostly motor neurons that harbour ALS-causative *C9orf72* hexanucleotide repeat expansions (HRE) [33]. This dataset contained two *C9orf72*-ALS patient lines and corresponding corrected control lines, in which the HRE were excised (Fig. 4a). Following DEA and GSEA, we identified 609 biological processes that were regulated with the *C9orf72* HRE. Comparison with our *FUS*-ALS sets revealed that 601 of these biological processes were uniquely regulated in the *C9orf72* dataset. The *FUS*-ALS LOF set did not overlap with this dataset at all and thus it could not support a role of these processes in *C9orf72*-ALS (Fig. 4e). However, the *FUS*-ALS GOF set shared eight biological processes with the *C9orf72* mutant motor neurons, including the downregulation of oxidative phosphorylation, upregulation of nuclear transport, establishment of organelle localization and negative regulation of execution phase of apoptosis (Fig. 4e,f). In conclusion, we find that *FUS* and *TARDBP* mutations trigger the dysregulation of many shared processes in motor neurons, several of which implicate dysfunctional mitochondrial energy metabolism. Comparison of our findings to motor neurons derived from *C9orf72*-ALS patient iPSCs on non-isogenic backgrounds, which can limit detectability, revealed early mitochondrial metabolic dysfunction as broadly shared pathway, strengthening the importance of our finding for ALS in general.

The downregulation of key mitochondrial pathways across isogenic ALS lines points to metabolic impairment

Our transcriptomic analysis consistently identified biological processes associated with mitochondrial energy metabolism across *in vitro*-derived ALS mutant motor neurons. Notably, 14 downregulated biological processes of the 45 shared among the *FUS*-ALS GOF and *TARDBP*-ALS motor neurons were processes linked to mitochondria. Mitochondrial dysfunctions have also been recognized as hallmarks of ALS pathology in patients as well as animal and cellular models.[33,51–55] We therefore decided to assess mitochondrial processes and pathways in more detail. At closer inspection, 54 of 123 mitochondrial respiratory genes were dysregulated in motor neurons in at least one ALS line (FUS or TDP-43) compared to the control at a cut-off of $p_{adj} < 0.001$. Most of these genes were downregulated in ALS motor neurons and spanned respiratory complexes I–V (Fig. 5a). In GSEA, we looked into three mitochondrial pathways that were specifically downregulated in ALS motor neurons (Fig. 5b,d,f) and the expression of selected genes within these biological pathways (Fig. 5c,e,g). For the GO term "ATP synthesis-coupled electron transport" the associated genes were mostly downregulated across ALS mutations (Fig. 5b), which is illustrated by its members *COX6A1*, *NDUFS6*, and *NDUFA12* (Fig. 5c). For "Oxidative phosphorylation" (Fig. 5d), *ATP5MF*, *COX7C*, and *NDUFB9* were clearly downregulated (Fig. 5e). Among the 37 mitochondrially encoded genes, the majority were downregulated across ALS mutations (Fig. 5f), exemplified by *MT-CO3*, *MT-ND3*, and *MT-ATP6* (Fig. 5g). This analysis highlights the various mitochondrial changes that occur in ALS mutant motor neurons, across *FUS* and *TARDBP* mutations. Altogether the downregulation of these mitochondrial genes suggests that oxidative respiration is compromised early on in *in vitro*-derived ALS motor neurons.

Mitochondrial energy metabolism is disturbed in motor neurons across ALS-causative mutations

In order to functionally assess mitochondrial activity and energy metabolism in ALS motor neurons, we performed *in vitro* differentiation according to the homogenous protocol that yields mostly spinal motor neurons. We used all the lines subjected to single cell RNA sequencing (Fig. 1 & Fig. 2). In addition, we included an isogenic FUS R244C line to investigate if mitochondrial dysfunction correlates with cytoplasmic mis-localization, because this

mutation does not show cytoplasmic mis-localization, but remains nuclear in motor neurons mutation and causes later onset of ALS than the FUS P525L (Extended Data Fig. 4a,b).[6] The bioenergetic profile of motor neurons was assessed using a Seahorse XF96 extracellular flux analyzer on day 21 after seeding, a time-point at which motor neurons have become metabolically active and separate well into small clusters (Fig. 6a). A series of specific mitochondrial drugs (Extended Data Fig. 6a) was administered to dissect mitochondrial mechanisms in real-time, measured as oxygen consumption rate (OCR) and extracellular acidification rate (ECAR) (Extended Data Fig. 6b,c). The aggregated runs of three independent differentiations with isogenic control and mutant motor neurons are presented in Extended Data Fig. 6d. Basal cellular respiration was significantly reduced in FUS R495X, FUS P525L homozygous and TDP-43 M337V motor neurons (Extended Data Fig. 6e), mainly due to a strong reduction in mitochondrial respiration (Fig. 6b), but not non-mitochondrial respiration (Extended Data Fig. 6f). Notably neither the *FUS* knockout, nor the nuclear FUS R244C line (Extended Data Fig. 4a,b), showed significant reduction in mitochondrial respiration (Fig. 6b), indicating that this phenotype is a function of FUS GOF and cytoplasmic mislocalization. Basal mitochondrial respiration was dissected into ATP-linked (Fig. 6c) and proton leak respiration (Extended Data Fig. 6g), revealing a similar pattern with significant reductions in FUS R495X, FUS P525L homozygous, and TDP-43 M337V motor neurons. To assess the bioenergetic capacity of motor neurons to respond to acutely high energy drains similar to what is seen during electric excitation, maximum substrate oxidation was induced using a mitochondrial uncoupler. Importantly, the pattern of reduced respiration was observed in FUS R495X, FUS P525L homozygous, and TDP-43 M337V motor neurons (Fig. 6d), demonstrating limited ability of these neurons to respond to high energy demands. Glycolytic acidification rates, after correction for non-glycolytic rates (Extended Data Fig. 6i), were determined to estimate glycolytic ATP production across motor neuron lines. These measurements revealed comparable basal rates, except for a significant reduction in FUS R495X motor neurons (Fig. 6e, Extended Data Fig. 6h). Upon induction of glycolysis by blocking mitochondrial ATP production with oligomycin, glycolytic capacity remained lower in FUS R495X motor neurons (Fig. 6f). OCR and ECAR were used to calculate the contribution of oxidative phosphorylation and glycolysis to the total ATP turnover. These analyses showed that the glycolytic contribution remains stable across lines, but significant reductions in mitochondrial ATP production were invoked in the FUS R495X, FUS P525L homozygous, and TDP-43 M337V

motor neurons (Fig. 6g). Thus, ATP homeostasis is compromised due to defects in oxidative phosphorylation in these ALS motor neurons, which is not compensated for by glycolysis. Thus, ALS-causative impairment in oxidative phosphorylation disables motor neurons to meet high energetic demands in FUS R495X, FUS P525L homozygous, and TDP-43 M337V mutant lines. In contrast, FUS P525L heterozygous and FUS R244C homozygous lines, that show less or no mis-localization of FUS, respectively, do not display such phenotypes. Collectively, bioenergetics profiling provides compelling evidence that cytoplasmic protein mis-localization gives rise to reduced mitochondrial activity in *FUS*-ALS and *TARDBP*-ALS lines.

Impaired mitochondrial motility is seen across ALS mutant motor axons

Because mitochondrial metabolism in several ALS motor neurons was reduced at basal rates, we wondered if part of these differences may be explained by dysfunction in the subcellular distribution of mitochondria. The main subcellular compartment in motor neurons is the axon, that encompasses an estimated 98% of the neuronal cytoplasm in adult humans, and the axonal transcriptome of motor neurons is highly enriched in genes involved in the mitochondrial respiratory chain compared to the soma.[37] Furthermore, frequently spaced mitochondria are required for normal axonal function, especially electrical signal transduction. In our *in vitro* derived motor neurons using the homogenous protocol, axons can grow to more than 2 mm by day 28 if we seed embryoid bodies with motor neuron progenitors, followed by terminal differentiation and maturation during which motor axons grow radially and continuously outwards (Fig. 7a). In order to assess mitochondrial motility in these axons, we imaged live neurons following a staining with a mitochondrial tracking dye (Fig. 7b-d). This allowed us to assess the movement of mitochondria along the anterograde-retrograde axonal axis in live cell time lapse microscopy (Fig. 7e). We recorded axons during six min time lapses at 0.5 Hz and tracked mitochondria using TrackMate 7.[56] Across motor neuron lines, we tracked 14,855,019 spots (total number of mitochondria in all frames) in this manner and assembled 459,479 individual track branches (total mitochondria over the time-lapses). Based on their movement, we classified mitochondria into stationary/oscillating mitochondria, mitochondria that move in anterograde or retrograde direction, while we discarded stray movements orthogonal to the axons. Thus, we found that FUS R244C, FUS R495X, FUS P525L (heterozygous and homozygous), as well as TDP-43 M337V motor neurons

displayed an increased number of stationary mitochondria compared to control motor neurons, unlike the FUS KO line (Fig. 7f), which was also reflected in a decrease of motile mitochondria in the anterograde and retrograde direction (Fig. 7g). The change in mitochondrial motility was significantly associated with the mutations (Pearson's χ^2 test, $\chi^2 = 88192$, $df = 12$, $p < 2.2e\text{-}16$). We found that stationary mitochondria were strongly overrepresented in ALS motor neurons, while they were underrepresented among control and *FUS* KO motor neurons (Fig. 7h). This analysis of mitochondrial motility indicates further disturbance of mitochondria across ALS lines, which are linked to GOF toxicity. As we see the dysfunction in mitochondrial motility also in FUS R244C motor neurons this defect does not seem directly linked to protein mis-localization. Collectively, we identify early defects in mitochondrial respiration, ATP turnover and mitochondrial motility in ALS motor neurons across *FUS* and *TARBP* mutants which could put these cells at particular risk.

Discussion

Motor neurons are highly vulnerable to degeneration in ALS and show early loss of synapses with skeletal muscle.[57] In order to understand the intrinsic mechanisms that could lead to their early demise across disease etiologies, we compared the impact of ALS mutations in *FUS* and *TARDBP* on the transcriptomes of *in vitro*-derived spinal motor neurons and interneurons at single cell resolution. Isogenic lines allowed us to detect subtle transcriptomic changes that could easily have been masked in lines with diverse genetic backgrounds, even if compared with corrected controls for each non-isogenic line. Motor neurons responded to *FUS* and *TARDBP* mutations with a much greater transcriptional dysregulation than interneurons, which mirrors their higher susceptibility to intrinsic pathological mechanisms in ALS. Our findings in FUS and *TARDBP* lines are complemented and corroborated by similar results in neurons specified from familial C9orf72- and sporadic ALS patient iPSCs that demonstrated a lesser transcriptional response in V2a and V1 Renshaw interneurons compared to susceptible motor neurons.[58] While interneurons are more resilient to ALS than most motor neurons *in vivo,* also glutamatergic V2a interneurons in the brainstem and spinal cord degenerate but only at late stages in the disease, which aggravates respiratory failure.[41] It is therefore likely that our analysis detects an early dysfunction in motor neurons specifically that could be at the heart of why they display higher intrinsic vulnerability in response to ALS mutations.

In motor neurons, we observed that individual *FUS* mutations elicit distinct, but also shared transcriptomic signatures. Cross comparison of FUS R495X and P525L with FUS KO motor neurons allowed us to dissect the contribution of LOF and GOF in FUS to this shared transcriptional signature, the majority of which is associated with a potentially toxic GOF. The shared GOF might arise due to the mis-localization of FUS, given that the R495X and P525L mutations ablate FUS' nuclear localization signal, resulting in its accumulation in the cytoplasm, as we also observe in our motor neurons. Cytoplasmic mutant FUS displays toxic GOF properties across cellular models, including the sequestration of various RNA species and proteins.[5,6,12] Although we only detect few ALS-FUS linked LOF pathways, they mirror defects in dendrites in rodents with FUS depletion or overexpression of ALS mutations[59–61] and potentially compensatory changes in splicing regulation because FUS is a non-essential factor in neurogenesis after all.[62] While the loss of FUS does not elicit motor neuron disease on its own[62] the interplay of GOF and LOF associated changes in *FUS*-ALS might exacerbate the course of the disease as in late stages the abundant cytoplasmic FUS aggregates also sequester nuclear FUS (two-hit hypothesis).[5,63,64] So far little is known about the contribution of these processes across different cell types, let alone spinal motor neurons. Our analysis of mutant FUS motor neurons affirms that LOF changes are indeed less pronounced than GOF changes. This is potentially due to the fact that the FUS protein belongs to the FET family of proteins that share similar functions and hence EWS and TAF15 might partially compensate for the loss of FUS in the context of nuclear depletion.[65,66] The small shared dysfunctions we identified across *TARDBP* and *C9orf72* datasets belonged only to GOF. In ALS patient tissue, *C9orf72*- and *TARDBP*-ALS converge on cytoplasmic TDP-43 aggregation and thus it may be anticipated there would be greater convergence across these lines than for *TARDBP*- and *FUS*-ALS. When aggregation starts is unknown, but it relies on other dysfunctions that develop over time. C9orf72 and TDP-43 motor neurons derived from iPSCs do not show obvious signs of TDP-43 mislocalization as they are in a very early phase of pathology. Nevertheless, early dysfunction in multiple cellular processes is apparent in such neurons,[27,33,45,67,68] which highlights that TDP-43 aggregation is not an early event in ALS. Neither is it required for degeneration as shown in model systems phenotype.[22,23] Thus, any convergence based on protein aggregation is not to be anticipated this early on in disease. Furthermore, as the *C9orf72* patient lines used have a different genetic background compared to our isogenic

lines, is possible that subtle converging dysfunctions that could have been detected in isogenicity are lost, particularly as differences between individuals are known to drive variation in iPSCs, both in differentiation capacity and morphology.[69]

Our cross-comparison with the bulk sequencing data from *C9orf72*-ALS patient derived motor neurons reveals unique responses but also further narrowed the signature of dysregulated genes that we detected in mutant *FUS* and *TARDBP* motor neurons. This signature contains transcriptional changes that are broadly shared among familial ALS motor neurons derived *in vitro* and might contain early converging pathological pathways. In this group, we identified the ablation of mitochondrial respiration as an early and broad pathological stage across disease causations. Mitochondria are central organelles for oxidative phosphorylation, lipid biogenesis, calcium homeostasis, and apoptosis. Their proper function and spacing is crucial in motor neurons with their exceptionally high demands for local energy supply and calcium buffering during electric signal transduction. Dysfunctional mitochondria are a hallmark of ALS found in end stage patient tissues.[70,71] Perturbations found across ALS model systems encompass changes in energy metabolism, mitochondrial motility and morphology.[55] In ALS motor neurons derived from familial ALS iPSC lines with *SOD1*, *TARDBP* and *C9orf72* mutations or sporadic ALS iPSCs mitochondrial respiration was impaired, but not in FUS patient lines investigated so far.[31,33,72,73] In our motor neurons, the cellular respiration was compromised only with specific *FUS*-ALS mutations. Using the aggressive homozygous FUS R495X and P525L mutations, we find a lower mitochondrial respiration of motor neurons already at an early stage. Furthermore, in our isogenic ALS motor neurons we found a pattern of metabolic dysfunction that is suggestive of a causal link with the dosage of cytoplasmic FUS as exemplified by the different mitochondrial respiratory rates in FUS P525L heterozygous and homozygous lines. Indeed, the homozygous mutant motor neurons with higher amounts of cytoplasmic FUS (R495X, P525L) were impaired in contrast to nuclear FUS R244C, FUS KO, and control motor neurons. Cytoplasmic FUS dosage might also explain why previously assessed patient derived heterozygous FUS P525L motor neurons had neither metabolic reduction nor mitochondrial deformations at similar experimental time-points following careful characterisation.[73]

Thus, our metabolic characterization of the *FUS* and *TARDBP* lines uncovers altogether a deeper link across ALS causation than was previously missing and demonstrates that

cytoplasmic FUS levels encumber mitochondrial respiration early on. In a longitudinal study of the FUS Δ14 mouse model, mitochondrial dysregulation was detected at onset of symptoms at age of 12 month but not earlier in bulk spinal cord samples.[74] Given the young biological age of iPSC-derived neurons[58,75] in our transcriptomic analysis at single cell resolution, one could infer that mitochondrial dysfunction might begin much earlier before onset of symptoms.

There is some evidence that *FUS* and *TARDBP* can both directly modulate mitochondria in ALS. Cytoplasmic FUS condensates were highly enriched for mitochondrial proteins,[76] but FUS mis-localization can also indirectly interfere with mitochondria by sequestering crucial mitochondrial components e.g. such as DHX30 required for translation of mitochondrial mRNAs, which hampered the renewal of the respiratory complexes.[77] A small fraction of cellular TDP-43 localizes to mitochondria and the prevention of the mitochondrial localization of TDP-43 M337V in mice ablated mitochondrial dysfunction.[78] Due to its partial mitochondrial localization, TDP-43 protein can interact with multiple crucial mitochondrial proteins and mRNAs, including prohibitin-2 (PHB2), VDAC1,[79] and *MT-ND3* and *MT-ND6* mRNAs.[53] PHB2 is important for mitochondria in neurons and its loss caused mitochondrial instability and neurodegeneration.[80,81]

Among ALS mutations in *FUS* and *TARDBP*, we found a significant and early reduction in motile mitochondria in distal axons, in agreement with previous findings.[32,33,67,82] We also observed impaired trafficking of mitochondria in FUS R244C motor neurons, which indicates that mis-localization of FUS might not underly the motility defect alone. The R244C mutation is defective in DNA repair function of FUS,[83,84] and earlier work in iPSC-derived motor neurons suggested nuclear genomic stress can act upstream of FUS aggregation and exacerbate axonal mitochondrial dysfunction[82] and represent mitochondrial replication defects found also in ALS patients.[85] The FUS mutations that we used also differ in their RNA binding ability due to their disposition of RGG domains which also modulate their ability for liquid-liquid phase transition.[86] There is still ambiguity how mitochondrial respiration and motility relate to each other in neurons. Our data suggests that different mechanisms could direct defects in mitochondrial motility and metabolism. The mis-localized proteins in ALS can also have a direct impact on axonal transport by binding to motor proteins and the axonal cytoskeleton

that could explain part of the motility phenotype. For example, cytoplasmic FUS associates directly with both myosin Va[87] and KIF5[88] but also regulates the mRNA of several motor proteins, including *KIF5C*, *KIF1B*, *KIF3A.*[89] Likewise, TDP-43 binds to various cytoskeletal proteins and regulates the *MAP1B* and *NEFL* mRNAs,[90] important components of the neuronal cytoskeleton. Furthermore *C9orf72*-derived dipeptides can road-block transport on microtubules resulting in arrested mitochondria.[91]

Altogether the combined mitochondrial dysfunction we observe could become detrimental to motor neurons over time. Motor neurons are exceptionally vulnerable to energy depletion. One of the main reasons for this is that motor neurons are highly dependent on transport along their long axons, which can span over a meter to reach muscle targets in arms, legs, feet and hands. Furthermore, synapses such as the neuromuscular junction are major sites of neuronal energy consumption and the trafficking of mitochondria to the synapses is thus critical to meet energy requirements of signaling.[91,92] Indeed, it has been estimated that 400-800 × 10^6 ATP molecules are required just to restore the electrochemical gradient of a neuron after a single action potential via Na^+/K^+ pumping.[93–96] Mitochondria have been estimated to generate 93% of the ATP in presynaptic terminals[97] and synapse physiology is clearly affected by local mitochondrial ATP production as local inhibition of oxidative phosphorylation or depletion of mitochondria here results in defective mobilization of synaptic vesicles, and failed neurotransmission.[98–100] Thus, the defects we find in mitochondrial respiration and ATP production could quickly lead to severe dysfunction and miscommunication with muscles and weakening of synapses. Concomitantly, it was recently shown that targeting mitochondria with a small molecule could improve upper motor neuron health in a TDP-43 mouse model.[101] The inability of ALS motor neurons to respond to high energy drains and the lack of compensatory glycolysis could render the motor neurons intrinsically more vulnerable as well as more dependent on glial support.[102,103]

Our data implicate mitochondria as important early targets in lower motor neurons. It has been shown that mitochondrial transport along axons is defective in iPSCs models of familial ALS,[32,33,67] but it has not been investigated what regulates this disturbance and how it affects the neuromuscular junction and communication between motor neurons and muscle. ATP is also thought to be used as a hydrotrope to help solubilize hydrophobic proteins. Thus, ATP concentrations could influence processes such as protein aggregation or liquid-liquid phase

separation,[104] events that both occur in ALS and are thought to be detrimental to motor neurons at late stages of the disease.

In conclusion, we find an intrinsic and early transcriptomic signature of dysfunction across ALS motor neurons derived from human iPSCs along with defective mitochondrial metabolism affecting the capability of motor neurons to respond to high energy drains. In addition, mitochondria are less motile implicating exhaustion of axonal energy supply and decline of proper function over time. Our study points out mitochondria as an early and pivotal target to modulate in ALS.

Methods

Antibodies

Custom mouse monoclonal antibodies against the FUS C-termini were generated at Boster Bio (Pleasanton, CA, USA) with antigens of wild-type P525 (N-DSRGEHRQDRRERPY-C; clone P3-A6C4) or mutant P525L (N-CGKMDSRGEHRQDRRERLY-C; clone P1-E7B6). The custom rabbit anti-FUS (N-terminus) antibody was described.[105] The custom rabbit anti-CPSF2 (CPSF-100) was described.[34] Other antibodies used in this study were: mouse monoclonal anti-FUS 4H11 [Santa Cruz Biotechnology, sc-47711], mouse anti-GAPDH 6C5 [Santa Cruz Biotechnology, sc-32233], rabbit anti-TARDBP [Proteintech Group, 12892-1-AP], mouse anti-TARDBP clone 41-7.1 [Santa-Cruz Biotechnologies, sc-100871], rat anti-TARDBP (phospho-S409/S410) clone 1D3 [Sigma-Aldrich, MABN14], mouse anti-OCT3/4 [Santa Cruz Biotechnology, sc-5279], rabbit anti-NANOG H155 [Santa Cruz Biotechnology, sc-33759], mouse anti-TUBB3 clone Tuj1 [Biolegend, 801202], mouse anti-ISL1/2 clone 39.4D5 [DSHB, 39.4D5-c], rabbit anti-ISL1 [Abcam, ab20670], and mouse anti-Hb9 (MNX1) clone 81.5C10 [DSHB, 81.5C10-c]. Secondary antibodies were donkey anti-rabbit IgG IRDye 800CW [Li-Cor, 926-32213], donkey anti-mouse IgG IRDye 800CW [Li-Cor, 926-32212], donkey anti-rabbit IgG IRDye 680LT [Li-Cor, 926-68023], donkey anti-mouse IgG IRDye 680LT [Li-Cor, 926-68022], donkey anti-mouse IgG AlexaFluor 488 [Invitrogen, A-21202], donkey anti-rat IgG AlexaFluor 488 [Invitrogen, A48269 and A21208], donkey anti-rabbit IgG AlexaFluor 546 [Invitrogen, A10040], donkey anti-rabbit IgG AlexaFluor 647 [Invitrogen, A31573], goat anti-rabbit IgG AlexaFluor 488 [Invitrogen, A21206], goat anti-mouse IgG2a AlexaFluor 488 [Invitrogen, A21131], goat anti-mouse IgG2b

AlexaFluor 488 [Invitrogen, A21141], goat anti-mouse IgG1 AlexaFluor 568 [Invitrogen, A21124], goat-anti-mouse IgG2a AlexaFluor 568 [Invitrogen, A21134], goat anti-mouse IgG2a AlexaFluor 647 [Invitrogen, A21241], goat anti-mouse IgG2b AlexaFluor 647 [Invitrogen, A21242], and goat anti-rabbit IgG AlexaFluor 405 [Invitrogen, A31556].

Plasmids

pCRISPR-EF1a-eSpCas9(1.1) was described in.[34] To generate the pCRISPR-EF1a-eSpCas9(1.1)-R495 plasmids two complementary oligonucleotides (sre326: 5'-CAC CGG GAC CGT GGA GGC TTC CGA-3', sre327: 5'-AAA CTC GGA AGC CTC CAC GGT CCC-3') or (sre324: 5'-CAC CGG ACC GTG GAG GCT TCC GAG-3', sre325: 5'-AAA CCT CGG AAG CCT CCA CGG TCC-3') and for M337 (JBA1: 5'-CAC CGC AGC ACT ACA GAG CAG TTG-3', and JBA2: 5'-AAA CCA ACT GCT CTG TAG TGC TGC-3') were subsequently phosphorylated using T4 polynucleotide kinase (PNK), annealed by heating to 95 °C and cooling to room temperature creating 5'-overhangs on both ends that were used to ligate into the BbsI sites of pCRISPR-EF1a-eSpCas9(1.1). Both, the FUS R495X and TDP-43 M337V donor plasmids containing disease-linked and silent mutations were ordered by gene synthesis in pUC57 [General Biosystems] and encompass homology arms of 800 bp upstream and 800 bp downstream and 808 bp upstream and 815 bp downstream of the cleavage site, respectively. The pRR-EF1a-Puro FUS R495 plasmid was ordered by gene synthesis [General Biosystems]. To generate pRR-Puro TARDBP M337 two oligos containing the CRISPR/Cas9 target site (mdr789: 5'-CGC AGC ACT ACA GAG CAG TTG GGG GAC GT-3' and mdr790: 5'-CCC CCA ACT GCT CTG TAG TGC TGC GAG CT-3') were phosphorylated using T4 PNK, annealed by heating to 95 °C and cooling to room temperature creating 5' overhangs on both ends which were used to ligate the annealed oligos into the SacI, AatII sites of pRR-Puro.[34,106] All plasmid sequences were confirmed by Sanger Sequencing.

Human induced pluripotent stem cell (iPSC) culture

Human iPSC lines were maintained with daily media changes in mTeSR1 or mTeSR-Plus medium (Stem cell Technologies, 85870 or 05825) as adherent cultures on plates coated with Matrigel (Corning, 354277) in a humid 5% CO_2 atmosphere at 37 °C. For passaging, they were treated with 10 µM Y-27632 (Tocris, 1254) for 1 hour and detached in DPBS (ThermoFisher,

14190250) with 0.5 mM EDTA (ThermoFisher, 15575020) or ReLeSR (Stemcell Technologies, 05872). The Y-27632 treatment was maintained until the next media change.

Genome editing

The DF6-9-9T.B control iPSC[107] (Wicell) were used to introduce all mutations. The generation of FUS KO and FUS P525L iPSC lines has been described before[12,34] and genome editing was essentially performed as described therein. In short, to introduce the R495X mutation in exon 14 of the *FUS* gene two pCRISPR-EF1a-eSpCas9(1.1)-R495 plasmids coding for the sgRNAs targeting the sequences 5'-GGG ACC GTG GAG GCT TCC GAG GG-3' and 5'-GGA CCG TGG AGG CTT CCG AGG GG-3' were used. To introduce the M337V mutation in exon 6 of the *TARDBP* gene a pCRISPR-EF1a-eSpCas9(1.1)-M337 plasmid coding for the sgRNA targeting the sequence 5'-GCA GCA CTA CAG AGC AGT TGG GG-3' was used. One day before transfection, 10 µM Y-27632 [Stemcell Technologies] and 2 µM Pyrintegrin [Stemcell Technologies] were added to the stem cell media. On the day of transfection, 6 wells of a 6-well plate with 90% confluent parental control hiPSC in mTeSR1 containing Y-27632 and Pyrintegrin were transfected with TransIT-LT1 Transfection Reagent [Mirus] for the FUS R495X and Lipofectamine 3000 for TDP-43 M337V [Life Technologies] according to the manufacturer's instructions. For the FUS R495X editing, each well was transfected with a total amount of 4.67 µg of DNA, transfecting 190 ng of pRR-EF1a-Puro-R495 and 4480 ng of a mix of pCRISPR-EF1a-SpCas9-R495 (both targets mixed 1:1) and the R495X donor plasmid for HDR. For each well a different molar ratio of pCRISPREF1a-SpCas9 R945 and donor plasmid was used (1:1, 1:3, 1:6, 4:1, 3:1, 2:1).

24 hours post transfection, the medium was changed to mTeSR1 supplemented with the 5 µl of the HDR-enhancer L755507 [Sigma], 10 µM Y-27632, and 2 µM Pyrintegrin. 48 hours post transfection, a single cell suspension was generated using Accutase [Thermo Fisher] and cells from the individual wells were pooled on a 15-cm plate in mTeSR1 containing 10 µM Y-27632 and 2 µM Pyrintegrin supplemented with 0.5 µg/ml Puromycin. Selection was maintained for one more day and Y-27632 and Pyrintegrin were maintained for four more days. Thereafter, colonies growing from single cells were picked and gDNA was isolated for clone screening using TRIzol [Thermo Fisher] according to the manufacturer's instructions. The R495 and M337 genomic loci were amplified from the genomic DNA using the KAPA Taq ReadyMix PCR

Kit according to the manufacturer's instructions using primers sre10: 5'-GTG GCT CTC ACA TGG GTA AG-3', and sre11: 5'-AAA GAC CCA GAG TGG CTA AG-3' for the R495 as well as P525L locus, and sre328: 5'-GAA TCA GGG TGG ATT TGG TAA TAG C-3' and sre331: 5'-AAT TCC CAC CAT TCT ATA CC-3'. The PCR products were purified over a preparative agarose gel using the Wizard SV Gel and PCR Clean-Up System [Promega]. Purified PCR products were sequenced at Eurofins genomics with sre125: 5'-GGG TGA TCA GGA ATT GGA AGG-3' for FUS P525L, sre11: 5'-AAA GAC CCA GAG TGG CTA AG-3' for FUS R495X, and sre270: 5'-TGG GTG GTG GGA TGA ACT TTG-3', respectively. PSC genomic stability was assessed by screening with the hPSC Genetic Analysis Kit (StemCell Technologies; #07550) which did not indicate the presence of any genomic abnormalities. Subsequent assessment with digital karyotyping (KaryoStat, ThermoFisher) highlighted the presence of a partial duplication of chromosome 14 in all cell lines, confirming comparable karyotypes across the isogenic lines.

In vitro differentiation to heterogenous spinal neurons

Adherent human iPSCs were grown to near confluence before the differentiation to heterogenous spinal/hindbrain neurons was initiated by changing the media for two days to media d1-2 (200 nM LDN193189 [Tocris, 6053], 10 µM SB431542 [Tocris, 1614], 25 ng/mL SHH-C25II [R&D Systems, 464-SH-025], 250 nM Purmorphamine [Tocris, 4551], 1 µM retinoic acid [Sigma-Aldrich, R2625]), followed by seven days medium d3–9 (Medium d1-2 with 3 µM CHIR99021 [Tocris, 4423]), one day of medium d10 (Medium d3–9 with 200 µM ascorbic acid [Sigma-Aldrich, A4403], 125 µM db-cAMP [Tocris, 1141], 2.5 µM DAPT [Tocris, 2634], 10 ng/mL each of BDNF [R&D Systems, 248-BD-025], GDNF [R&D Systems, 212-GD-010], NT-3 [R&D Systems, 267-N3-025], and CNTF [R&D Systems, 257-NT-010]), and three days of medium d11–13 (3 µM CHIR99021, 25 ng/mL SHH-C25II, 250 nM Purmorphamine, 1 µM retinoic acid, with 200 µM ascorbic acid, 125 µM db-cAMP, 2.5 µM DAPT, 10 ng/mL each of BDNF, GDNF, NT-3, and CNTF). From day 14 onwards, the neuronal culture was maintained in medium d14+ (200 µM ascorbic acid, 125 µM db-cAMP, 2.5 µM DAPT, 10 ng/mL each of BDNF, GDNF, NT3, and CNTF) until the experimental time-points or harvest.

In vitro differentiation to spinal motor neurons (homogenous protocol)

Specification of iPSC lines into spinal motor neurons was done as previously described,[37] and was adapted from Refs 32,35 and detailed also here. Specifically, embryoid bodies were formed and neural induction initiated (days 1-2) by resuspending iPSCs at 0.5-0.75 M cells/ml media in 50% v/v Neurobasal, 50% v/v DMEM/F12, 0.5% v/v N2 supplement, 1% v/v B-27 supplement, 5 µM Y-27632, 40 µM SB431542, 200 nM LDN193189, 3 µM CHIR99021, 200 µM ascorbic acid, followed by seven days (days 3-9) of ventralizing and caudalizing patterning in medium consisting of 50% v/v Neurobasal, 50% v/v DMEM/F12, 0.5% v/v N2 supplement, 1% v/v B-27 supplement, 200 µM ascorbic acid, 200 nM retinoic acid, 500 nM SAG [Tocris, 6390]. At day 10, the embryoid bodies were treated with 5 µM Y-27632 for 1 hour, washed with DPBS [ThermoFisher, 14190250], and then dissociated for 5-10 min with gentle titration in warm TrypLE Express [ThermoFisher, 12604021], supplemented with 5 µM Y-27632. After the embryoid bodies disband into single cells, they were collected by centrifugation at 200 g for 4 min, and resuspended in maturation medium consisting of Neurobasal, B-27 supplement, 200 µM ascorbic acid, 10 µM DAPT, 10 ng/mL of each GDNF [Peprotech, 450-10] and BDNF [Peprotech, 450-02] and 5 µM Y-27632. The cell suspension was filtered through cell strainer caps and motor neuron progenitors were seeded at >15,000 cells/cm^2 on plates coated with fibronectin [ThermoFisher, 33016015], poly-L-ornithine (Sigma-Aldrich, P4957), and laminin A (Sigma-Aldrich, L2020). The next day, the maturation media was replaced but Y-27632 was omitted. On day 12, remaining proliferative cells were eliminated with a 48 hours pulse of 2 µM 5-fluorodeoxyuridine [Sigma-Aldrich, F0503]. From day 14 onwards, the neuron culture was maintained in medium d14+ consisting of Neurobasal, B27 supplement, 200 µM ascorbic acid, 10 ng/mL each of BDNF and GDNF with media changes every other day.

Dissociation of neuronal cultures and single cell capture by FACS

Single cells from neuronal cultures were isolated as described.[108] Briefly, the adherent neuron cultures were treated with 5 µM Y-27632 (Tocris, 1254) for 1 hour. After washing carefully with HBSS (ThermoFisher, 14025050), the cultures were dissociated in TrypLE Express (ThermoFisher, 12604021), supplemented with 5 µM Y-27632 for 20-30 min under gentle agitation and with pipetting at 5 min intervals to break cell clumps apart. The dissociated

neurons were then collected by centrifugation at 200 g for 5 min and resuspended in 500 µL HBSS supplemented with 2% v/v B-27 supplement [ThermoFisher, 0080085SA], 2% v/v KnockOut Serum Replacement [ThermoFisher, 10828028], 2% w/v bovine serum albumin [Sigma-Aldrich, A9418-10G], 25 mM D-glucose [Sigma-Aldrich, G7021-100G], 5 µM Y-27632, 10 ng/mL BDNF [Peprotech, 450-02], 10 ng/mL GDNF [Peprotech, 450-10]. The cell suspension was then filtered through cell strainer caps into FACS tubes (BD Biosciences) and was kept on ice. The single cell suspensions were index sorted within an hour of harvest on a FACSAria III or FACSAria Fusion (BD Biosciences) at 4 °C and 20 psi through a 100 µm ceramic nozzle under sterile conditions. Based on TOPRO-3 iodide staining, dead cells were excluded and neurite fragments were removed by gates based on unstained live and stained dead-cell control samples. Single cells were collected into 96 multiwell plates (ThermoFisher, 11355960 and 10036339) by dispensing individual cells in 5 nL drops directly into 3 µL ice-cold single cell lysis buffer (scLB, 0.134% Triton X-100 [Sigma], 0.5 U/µL recombinant RNase inhibitor [Takara, 2313B], 3.33 mM each dNTP [ThermoFisher, R1121], 1 mM dithiothreitol [DTT, ThermoFisher], 1.67 µM Smarter-oligo-dTVN [Biomers.net], 6.7e-7 diluted ERCC Spike-In [ThermoFisher, 4456740]). After collection the plates were immediately sealed with adhesive sheets (ThermoFisher, AB0558) and snap frozen on dry ice.

Single cell RNA sequencing (Smart-Seq2)

We prepared single-cell cDNA libraries using Smart-Seq2[109] with adaptations as described. [108] Cell lysates were thawed on ice before denaturation at 72 °C for 3 min. Following primer annealing for 2 min on ice, 2.76 µL master mix 1 (1 µL 5x Superscript II reaction buffer [ThermoFisher], 1 µL 5 M betaine [Sigma-Aldrich], 0.25 µL 100 mM dithiothreitol (DTT), 0.035 µL 1 M magnesium chloride [ThermoFisher], 0.1 µL 100 µM Smarter-TSO [Biomers.net], 50 U SuperScript II reverse transcriptase, 5 U recombinant RNase inhibitor) was added per lysate. On a thermocycler, the first strand synthesis was carried out as follows: 90 min at 42 °C; 10 cycles of 2 min at 50 °C, 2 min at 42 °C; and 15 min at 70 °C before cooling to 4 °C. Then 7.5 µL master mix 2 (1.15 µL) was added per sample. On a thermocycler, the second strand synthesis and amplification were carried out as follows: 3 min at 98 °C; 21 cycles of 20 sec at 98 °C, 15 sec at 67 °C, 6 min at 72 °C; and 5 min at 72 °C before cooling to 12 °C. The single-cell cDNA libraries were purified with SPRI beads (SeraMag beads, in 19.5% w/v PEG 8000,

1 M sodium chloride, 10 mM Tris-HCl pH 8.0, 1 mM disodium EDTA, 0.01% v/v Igepal CA630, 0.25% w/v sodium azide). The samples were barcoded with unique Illumina Nextera Indexes using reagents from the Nextera Sample Preparation Kit. The final libraries were then combined at equimolar concentrations before purification of the pools with SPRI beads. Sequencing was performed on HiSeq 2000 (Illumina) and NovaSeq 6000 (Illumina) at NGI Sweden, Stockholm.

Single-cell RNA-Seq mapping and cell type classification

Raw sequencing reads were mapped to the hg38 human reference genome using STAR (version 2.7.0e)[110] with parameters "-outSAMstrandField" set to "intronMotif". Aligned reads were assigned to genomic locations with the 'rpkmforgenes.py' script,[111] using an annotation GTF file from Ensembl version 95 (GRCh38.95). In 'rpkmforgenes.py', the parameters "-fulltranscript" and "-rmnameoverlap" were used. After obtaining the raw counts, cells with < 100,000 uniquely mapped reads and/or < 5,000 detected genes were excluded. Genes with an RPKM value of > 1 were considered detected. Cells were classified as neurons based on expression of NEFM (neurofilament-medium) at > 100 RPKM and SNAP25 at > 10 RPKM. Neurons were further classified as motor neurons if they showed expression of at least one of the transcription factors *ISL1*, *ISL2* or *MNX1* at > 1 RPKM, combined with either *SLC18A3* (VAChT) or *SLC5A7* (ChT) at > 5 RPKM, but lacked expression of the interneuron markers VSX2 (< 1 RPKM) and SIM1(< 1 RPKM). All neuronal cells that were not classified as motor neurons were generically termed interneurons. V2a interneurons were neuronal cells that were positive for both *VSX2* (CHX10) and *SOX14* at > 1 RPKM.

Identification of differentially expressed genes and pathways

Differential expression analysis between groups was conducted in R (version 3.6.1)[112] using the *DESeq2* package (version 1.24.0).[113] Fit type was set to "local". An FDR-adjusted p-value of < 0.05 was considered significant. Gene set enrichment analysis was performed using the *fgsea* package version 1.8.0. DESeq2 outputs were ranked by test statistic to be used as input. These gene lists were compared to GO biological process pathways obtained from the human MsigDB collection (C5, GO-bp). Only pathways containing between 10-500 genes were considered in the analysis. UMAP plots, heatmaps and Venn diagrams were all generated in

R. UMAP plots were generated using *Seurat* (version 4.2.0)[114] using either all cells or all neuronal cells. Batch normalization was conducted in Seurat using canonical correlation analysis (CCA). The dataset was separated in batches for each biological experiment, which were separately normalized using SCTransform and re-integrated using integration anchors and integration features. The top 2,000 most variable gene features were used as integration features. Heatmaps were generated using the *pheatmap* package version 1.0.12. Venn diagrams were generated using the *Vennerable* package version 3.1.0 or the *venn* package version 1.11. Upset plots were generated using packages *ggplot2* (version3.4.1) and *ggupset* (version 0.3.0). For QIAGEN's Ingenuity Pathway Analysis (IPA)[43] the list of differentially expressed genes between mutant motor neurons and control was used as input. Genes with FDR < 0.1 were considered significantly differentially expressed for the pathway analysis and were compared to the Ingenuity Knowledge Base reference set (version Q4 2022, accessed on February 7, 2023). Canonical pathways across the different sample sets were ranked according to the FDR value aggregate of pathway enrichment across the *FUS*-ALS MN datasets (internally calculated by IPA). Heatmaps of significance (FDR value) and activation scores (z-score) for the 12 highest ranking canonical pathways were generated. Pathways with an FDR of < 0.1 were considered significantly enriched. For mapping expression changes to protein structures, RCSB PDB entries for mammalian mitochondrial respiratory complexes I (5lc5, *Bos taurus*), II (1zoy, *Sus scrofa*), III (1bgy, *B. taurus*), IV (1occ, *B. taurus*), and IV (5ara, *B. taurus*) were retrieved, arranged and rendered in UCSF Chimera (version 1.16, build 42360). The expression across human ALS motor neurons (mean $\log_2$ foldchange of ALS compared to control motor neurons) was used to color the individual orthologous protein chains using a python script, generated in R (version 4.2.0) together with the scale legend.

Immunofluorescence microscopy

For imaging of iPSCs, they were grown on 12-well chamber microscope slides [ibidi, 81201] and fixed with 4% paraformaldehyde for 20 min at room temperature. The cells were then washed three times for 5 min each with PBS and then permeabilized in TBS supplemented with 0.5% v/v Triton X-100 [AppliChem], 6% bovine serum albumin (BSA) [Sigma-Aldrich], in TBS for 30 min at room temperature. Primary antibody incubation was performed in antibody diluent (0.1% v/v Triton X-100, 6% w/v BSA, in TBS) overnight at 4 °C. The cells were washed

three time for 5 min with antibody diluent before being incubated with secondary antibodies in antibody diluent for 2 hours at room temperature. Subsequently, the cells were counterstained with 100 ng/ml DAPI in PBS for 10 minutes at room temperature and then washed twice for 5 min with PBS. Coverslips were then mounted using hard set antifade mounting medium [Vectashield, H-1400]. Images were acquired using an Eclipse Ti-2 epifluorescence microscope [Nikon] with a 20×/dry lens.

Neurons were grown on glass coverslips or in imaging grade 96-well plates (ibidi, 89626; IBL Austria, 220.230.042) coated with fibronectin [ThermoFisher, 33016015], poly-L-ornithine (Sigma-Aldrich, P4957), and laminin A (Sigma-Aldrich, L2020) for immunofluorescence microscopy. At indicated time-points, the neurons were washed with warm HBSS (containing magnesium and calcium chloride, ThermoFisher Scientific, 14025100), fixed in 4% w/v paraformaldehyde for 15 min, and washes three times with HBSS to end the fixation. Then, the neurons were permeabilized in blocking solution [0.5% w/v Triton X-100 (Sigma-Aldrich, X100-1L), 10% v/v normal donkey serum (Jackson ImmunoResearch, 017-000-121), in PBS (ThermoFisher Scientific, 70011044)] for 30 min. Primary antibodies were applied in fresh blocking solution over night at 4 °C. Following three washes with blocking solution over 30 min, secondary antibodies diluted in blocking solution were applied for 1.5 hours at room temperature in the dark. The neurons were washes twice with PBS (ThermoFisher Scientific, 70011044), followed by a single wash in ultrapure water (ThermoFisher Scientific, 10977049). The cells were mounted in Fluoromount G (ThermoFisher Scientific, 00-4958-02) and subjected to inverted confocal microscopy on an LSM700 (Zeiss) or LSM800-Airy microscope (Zeiss).

Western blotting

One 10-cm dish of iPSCs was harvested by incubation with DPBS-EDTA and pelleted by centrifugation at 200 g. Cell pellets were resuspended in 400 µl RIPA buffer [Sigma Aldrich, R0278-50ML] supplemented with 2x Halt protease and phosphatase inhibitor cocktail [Thermo Fisher Scientific, 78441], 2 mM manganese sulfate, and 25 U/ml Cyanase nuclease [Serva, 18542.02] followed by incubation on ice for 30 min with vortexing in 5-min intervals. 400 µl of 2x LDS loading buffer (ThermoFisher Scientific, NP0007) supplemented with 250 mM DL-dithiothreitol (Sigma-Aldrich, 43816-50ML) were added and samples were boiled

10 min at 70 °C. Samples were loaded on 4-12% Bolt Tris-Bis gels and ran with 1x MOPS buffer, followed by blotting on nitrocellulose membranes using the iBlot2 transfer device. Membranes were blocked for 1 hour in TBS-Tween (0.1%) supplemented with 5% w/v non-fat dry milk, followed by incubation with primary antibodies over night at 4 °C. After five subsequent washes with TBS-Tween (0.1%), secondary antibodies were added in TBS-Tween (0.1%) supplemented with 5% non-fat dry milk, incubated for 1.5 hours at room temperature, followed by five consecutive 5-minute washes with TBS-Tween (0.1%) and scanning of the membranes on an Odyssey CLx scanner [Li-Cor].

Extracellular flux XF96 Seahorse measurements

Human iPSC-derived motor neurons were differentiated according to the homogenous protocol and seeded at day 10 into Seahorse XF96-well plates (Seahorse Bioscience, Agilent Technologies). At day 21 the plates were washed and incubated for 60 min in an air incubator at 37 °C with Seahorse DMEM-based assay medium, supplemented with 25 mM glucose and 2 mM glutamine (pH adjusted to 7.5). The XF96 plate was then transferred to a temperature-controlled (37 °C) Seahorse extracellular flux analyzer (Agilent Technologies) and allowed a temperature equilibration period before assay cycles (consisting of 1-min mix, 2-min wait, and 3-min measure period). Oxygen consumption rates (OCR) and extracellular acidification rates (ECAR) were dissected into different functional modules as described in detail previously [115,116]. In brief, after four basal assay cycles oligomycin (5 µg/ml) was injected to inhibit the ATP synthase to determine OCR related to ATP synthesis for 3-6 cycles (lowest value of 3-6 cycles was used for calculation). 2,4-Dinitrophenol (2,4-DNP; 100 µM) was injected to stimulate maximal respiration, revealing maximal substrate oxidation capacity (3 cycles, highest value used for calculation). Next, rotenone (R, 4 µM) and antimycin A (AA, 2 µM) were added, followed by 3 assay cycles to determine the non-mitochondrial OCR (lowest of 3 values). Finally, 2-deoxy-glucose (2-DG, 100 mM) was added to determine glycolytic extracellular acidification rates (ECARs), subtracting the lowest of 6 ECAR measurements after 2-DG injection. ECAR values were transformed to PPR values using the machine settings. PPR values after 2-DG injection were subtracted to correct for non-glycolytic acidification. After the measurement, the cells were lysed and total dsDNA amount per well was determined

using Quant-iT PicoGreen dsDNA Assay Kit (ThermoFisher). All OCR and PPR values were normalized to 230 ng dsDNA (mean DNA content/well of all measurements).

Live cell imaging for tracking mitochondria

Motor neurons were derived using the homogenous protocol, but the embryoid bodies were attached at day 10 to imaging grade 24-well plates (ibidi, 82406) coated with fibronectin (ThermoFisher, 33016015), poly-L-ornithine (Sigma-Aldrich, P4957), and laminin A (Sigma-Aldrich, L2020) to promote axons outgrowth. The neurons were matured until at least day 27. For tracking mitochondria, motor neurons were cultured in Imaging Optimized BrainPhys medium (Stemcell Technologies, 05796) with SM1 NeuroCult supplement (Stemcell Technologies, 05711), 200 nM L-ascorbic acid (Sigma-Aldrich, A4403), and 10 ng/mL BDNF (Peprotech, 450-02) and 10 ng/mL GDNF (Peprotech, 450-10). After addition of 50 nM TMRM (ThermoFisher Scientific, I34361) mitochondria were labelled for 30 min before the medium was replaced. Live cell microscopy was performed in an Axio Observer 7 (Zeiss) equipped with a Plan Apo 40x/0.95 Ph3 objective and under a 5% CO_2 atmosphere at 37 °C. Four regions across distal axons were selected to record 5-min long time-lapses. For analysis of mitochondrial movement, individual mitochondria were traced in Fiji[117] using the TrackMate 7 extension with the StarDist detector[56] and a Sparse LAP tracker (as in 'mitotracker.py'). The mitochondrial traces were then annotated and analysed in R (version 4.2.0)[112] using our custom package 'mitotrackR' (https://github.com/schwi24/mitotrackR). Briefly, mitochondrial traces were split into branches to analyse mitochondria discernible over the time-lapse. Mitochondrial movement in the axonal direction was assigned using cone sections of a sphere with an internal angle of $2 \times \mathrm{acos}(1/3) \approx 141°$, that trisects the sphere into equal sections for classification of anterograde, retrograde, and orthogonal movement steps from the center. Stationary mitochondria were defined as discernible mitochondria that never exceed low migration speeds (maximal speed < 0.05 µm/s) or step in place so that they cover little distance over the time-lapse (summed up distance < 2 µm). Discernible mitochondria with overall orthogonal movement were excluded from the analysis. Statistical tests were performed in R (version 4.2.0).

Data Availability

We have deposited all raw and processed sequencing data generated in this study on the NCBI Gene Expression Omnibus (GEO) under the accession number GSE226482. The *C9orf72*-ALS bulk RNA sequencing data was retrieved directly from the authors of the study.[33]

References

1. Nijssen, J., Comley, L. H. & Hedlund, E. Motor neuron vulnerability and resistance in amyotrophic lateral sclerosis. *Acta Neuropathol* **133**, 863–885 (2017).
2. Schweingruber, C. & Hedlund, E. The Cell Autonomous and Non-Cell Autonomous Aspects of Neuronal Vulnerability and Resilience in Amyotrophic Lateral Sclerosis. *Biology (Basel)* **11**, 1191 (2022).
3. Swinnen, B. & Robberecht, W. The phenotypic variability of amyotrophic lateral sclerosis. *Nat Rev Neurol* **10**, 661–670 (2014).
4. DeJesus-Hernandez, M. *et al.* Expanded GGGGCC Hexanucleotide Repeat in Noncoding Region of C9ORF72 Causes Chromosome 9p-Linked FTD and ALS. *Neuron* **72**, 245–256 (2011).
5. Vance, C. *et al.* Mutations in FUS, an RNA processing protein, cause familial amyotrophic lateral sclerosis type 6. *Science* **323**, 1208–1211 (2009).
6. Kwiatkowski, T. J. *et al.* Mutations in the FUS/TLS Gene on Chromosome 16 Cause Familial Amyotrophic Lateral Sclerosis. *Science (1979)* **323**, 1205–1208 (2009).
7. Rosen, D. R. *et al.* Mutations in Cu/Zn superoxide dismutase gene are associated with familial amyotrophic lateral sclerosis. *Nature* **362**, 59–62 (1993).
8. Sreedharan, J. *et al.* TDP-43 Mutations in Familial and Sporadic Amyotrophic Lateral Sclerosis. *Science (1979)* **319**, 1668–1672 (2008).
9. Filézac de L'Etang, A. *et al.* Marinesco-Sjögren syndrome protein SIL1 regulates motor neuron subtype-selective ER stress in ALS. *Nat Neurosci* **18**, 227–38 (2015).
10. Vandoorne, T., De Bock, K. & Van Den Bosch, L. Energy metabolism in ALS: an underappreciated opportunity? *Acta Neuropathol* **135**, 489–509 (2018).
11. Renton, A. E., Chiò, A. & Traynor, B. J. State of play in amyotrophic lateral sclerosis genetics. *Nat Neurosci* **17**, 17–23 (2014).
12. Jutzi, D. *et al.* Aberrant interaction of FUS with the U1 snRNA provides a molecular mechanism of FUS induced amyotrophic lateral sclerosis. *Nat Commun* **11**, 6341 (2020).
13. Dormann, D. FUS cinating insights into motor neuron degeneration. *EMBO J* **35**, 1015–1017 (2016).
14. Scekic-Zahirovic, J. *et al.* Toxic gain of function from mutant FUS protein is crucial to trigger cell autonomous motor neuron loss. *EMBO J* **35**, 1077–97 (2016).
15. Sharma, A. *et al.* ALS-associated mutant FUS induces selective motor neuron degeneration through toxic gain of function. *Nat Commun* **7**, (2016).
16. Patel, A. *et al.* A Liquid-to-Solid Phase Transition of the ALS Protein FUS Accelerated by Disease Mutation. *Cell* **162**, 1066–1077 (2015).
17. Bowden, H. A. & Dormann, D. Altered mRNP granule dynamics in FTLD pathogenesis. *J Neurochem* **138**, 112–133 (2016).

18. Van Deerlin, V. M. *et al.* TARDBP mutations in amyotrophic lateral sclerosis with TDP-43 neuropathology: a genetic and histopathological analysis. *Lancet Neurol* **7**, 409–16 (2008).
19. Gitcho, M. A. *et al.* TDP-43 A315T mutation in familial motor neuron disease. *Ann Neurol* **63**, 535–8 (2008).
20. Kabashi, E. *et al.* TARDBP mutations in individuals with sporadic and familial amyotrophic lateral sclerosis. *Nat Genet* **40**, 572–4 (2008).
21. Yokoseki, A. *et al.* TDP-43 mutation in familial amyotrophic lateral sclerosis. *Ann Neurol* **63**, 538–42 (2008).
22. Igaz, L. M. *et al.* Dysregulation of the ALS-associated gene TDP-43 leads to neuronal death and degeneration in mice. *J Clin Invest* **121**, 726–38 (2011).
23. Wegorzewska, I., Bell, S., Cairns, N. J., Miller, T. M. & Baloh, R. H. TDP-43 mutant transgenic mice develop features of ALS and frontotemporal lobar degeneration. *Proc Natl Acad Sci U S A* **106**, 18809–14 (2009).
24. Ling, J. P., Pletnikova, O., Troncoso, J. C. & Wong, P. C. TDP-43 repression of nonconserved cryptic exons is compromised in ALS-FTD. *Science* **349**, 650–5 (2015).
25. Ma, X. R. *et al.* TDP-43 represses cryptic exon inclusion in the FTD-ALS gene UNC13A. *Nature* **603**, 124–130 (2022).
26. Brown, A.-L. *et al.* TDP-43 loss and ALS-risk SNPs drive mis-splicing and depletion of UNC13A. *Nature* **603**, 131–137 (2022).
27. Klim, J. R. *et al.* ALS-implicated protein TDP-43 sustains levels of STMN2, a mediator of motor neuron growth and repair. *Nat Neurosci* **22**, 167–179 (2019).
28. Arai, T. *et al.* TDP-43 is a component of ubiquitin-positive tau-negative inclusions in frontotemporal lobar degeneration and amyotrophic lateral sclerosis. *Biochem Biophys Res Commun* **351**, 602–11 (2006).
29. Mackenzie, I. R. A. *et al.* Pathological TDP-43 distinguishes sporadic amyotrophic lateral sclerosis from amyotrophic lateral sclerosis with SOD1 mutations. *Ann Neurol* **61**, 427–34 (2007).
30. Neumann, M. *et al.* Ubiquitinated TDP-43 in frontotemporal lobar degeneration and amyotrophic lateral sclerosis. *Science* **314**, 130–3 (2006).
31. Fujimori, K. *et al.* Modeling sporadic ALS in iPSC-derived motor neurons identifies a potential therapeutic agent. *Nat Med* **24**, 1579–1589 (2018).
32. Guo, W. *et al.* HDAC6 inhibition reverses axonal transport defects in motor neurons derived from FUS-ALS patients. *Nat Commun* **8**, 861 (2017).
33. Mehta, A. R. *et al.* Mitochondrial bioenergetic deficits in C9orf72 amyotrophic lateral sclerosis motor neurons cause dysfunctional axonal homeostasis. *Acta Neuropathol* **141**, 257–279 (2021).
34. Reber, S. *et al.* CRISPR-Trap: a clean approach for the generation of gene knockouts and gene replacements in human cells. *Mol Biol Cell* **29**, 75–83 (2018).
35. Nijssen, J., Aguila, J., Hoogstraaten, R., Kee, N. & Hedlund, E. Axon-Seq Decodes the Motor Axon Transcriptome and Its Modulation in Response to ALS. *Stem Cell Reports* **11**, 1565–1578 (2018).
36. Maury, Y. *et al.* Combinatorial analysis of developmental cues efficiently converts human pluripotent stem cells into multiple neuronal subtypes. *Nat Biotechnol* **33**, 89–96 (2015).
37. Nijssen, J., Aguila, J. & Hedlund, E. Axon-seq for in Depth Analysis of the RNA Content of Neuronal Processes. *Bio Protoc* **9**, (2019).

38. Mackenzie, I. R. A. *et al.* Pathological heterogeneity in amyotrophic lateral sclerosis with FUS mutations: two distinct patterns correlating with disease severity and mutation. *Acta Neuropathol* **122**, 87–98 (2011).
39. Chen, L., Wang, Y. & Xie, J. A Human iPSC Line Carrying a de novo Pathogenic FUS Mutation Identified in a Patient With Juvenile ALS Differentiated Into Motor Neurons With Pathological Characteristics. *Front Cell Neurosci* **14**, 1–10 (2020).
40. Ichiyanagi, N. *et al.* Establishment of in Vitro FUS-Associated Familial Amyotrophic Lateral Sclerosis Model Using Human Induced Pluripotent Stem Cells. *Stem Cell Reports* **6**, 496–510 (2016).
41. Romer, S. H. *et al.* Accessory respiratory muscles enhance ventilation in ALS model mice and are activated by excitatory V2a neurons. *Exp Neurol* **287**, 192–204 (2017).
42. Salamatina, A. *et al.* Differential Loss of Spinal Interneurons in a Mouse Model of ALS. *Neuroscience* **450**, 81–95 (2020).
43. Krämer, A., Green, J., Pollard, J. & Tugendreich, S. Causal analysis approaches in Ingenuity Pathway Analysis. *Bioinformatics* **30**, 523–30 (2014).
44. Arnold, E. S. *et al.* ALS-linked TDP-43 mutations produce aberrant RNA splicing and adult-onset motor neuron disease without aggregation or loss of nuclear TDP-43. *Proc Natl Acad Sci U S A* **110**, E736-45 (2013).
45. Melamed, Z. *et al.* Premature polyadenylation-mediated loss of stathmin-2 is a hallmark of TDP-43-dependent neurodegeneration. *Nat Neurosci* **22**, 180–190 (2019).
46. Lagier-Tourenne, C. & Cleveland, D. W. Rethinking ALS: The FUS about TDP-43. *Cell* **136**, 1001–4 (2009).
47. Gordon, D. *et al.* Single-copy expression of an amyotrophic lateral sclerosis-linked TDP-43 mutation (M337V) in BAC transgenic mice leads to altered stress granule dynamics and progressive motor dysfunction. *Neurobiol Dis* **121**, 148–162 (2019).
48. Watanabe, S. *et al.* ALS-linked TDP-43M337V knock-in mice exhibit splicing deregulation without neurodegeneration. *Mol Brain* **13**, 13–16 (2020).
49. Mackenzie, I. R. A., Rademakers, R. & Neumann, M. TDP-43 and FUS in amyotrophic lateral sclerosis and frontotemporal dementia. *Lancet Neurol* **9**, 995–1007 (2010).
50. Ling, S. C., Polymenidou, M. & Cleveland, D. W. Converging mechanisms in als and FTD: Disrupted RNA and protein homeostasis. *Neuron* **79**, 416–438 (2013).
51. Ho, R. *et al.* ALS disrupts spinal motor neuron maturation and aging pathways within gene co-expression networks. *Nat Neurosci* **19**, 1256–1267 (2016).
52. Singh, T. *et al.* Neuronal mitochondrial dysfunction in sporadic amyotrophic lateral sclerosis is developmentally regulated. *Sci Rep* **11**, 1–16 (2021).
53. Wang, W. *et al.* The inhibition of TDP-43 mitochondrial localization blocks its neuronal toxicity. *Nat Med* **22**, 869–78 (2016).
54. Yu, C.-H. *et al.* TDP-43 Triggers Mitochondrial DNA Release via mPTP to Activate cGAS/STING in ALS. *Cell* **183**, 636-649.e18 (2020).
55. Smith, E. F., Shaw, P. J. & De Vos, K. J. The role of mitochondria in amyotrophic lateral sclerosis. *Neurosci Lett* **710**, 132933 (2019).
56. Ershov, D. *et al.* TrackMate 7: integrating state-of-the-art segmentation algorithms into tracking pipelines. *Nat Methods* **19**, 829–832 (2022).
57. Fischer, L. R. *et al.* Amyotrophic lateral sclerosis is a distal axonopathy: Evidence in mice and man. *Exp Neurol* **185**, 232–240 (2004).

58. Ho, R. *et al.* Cross-Comparison of Human iPSC Motor Neuron Models of Familial and Sporadic ALS Reveals Early and Convergent Transcriptomic Disease Signatures. *Cell Syst* **12**, 159-175.e9 (2021).
59. Groen, E. J. N. *et al.* ALS-associated mutations in FUS disrupt the axonal distribution and function of SMN. *Hum Mol Genet* **22**, 3690–3704 (2013).
60. Orozco, D. *et al.* Loss of fused in sarcoma (FUS) promotes pathological Tau splicing. *EMBO Rep* **13**, 759–764 (2012).
61. Sephton, C. F. *et al.* Activity-dependent FUS dysregulation disrupts synaptic homeostasis. *Proc Natl Acad Sci U S A* **111**, E4769-78 (2014).
62. Kino, Y. *et al.* FUS/TLS deficiency causes behavioral and pathological abnormalities distinct from amyotrophic lateral sclerosis. *Acta Neuropathol Commun* **3**, 24 (2015).
63. Dormann, D. *et al.* ALS-associated fused in sarcoma (FUS) mutations disrupt transportin-mediated nuclear import. *EMBO Journal* **29**, 2841–2857 (2010).
64. Vance, C. *et al.* ALS mutant FUS disrupts nuclear localization and sequesters wild-type FUS within cytoplasmic stress granules. *Hum Mol Genet* **22**, 2676–2688 (2013).
65. Svetoni, F., Frisone, P. & Paronetto, M. P. Role of FET proteins in neurodegenerative disorders. *RNA Biol* **13**, 1089–1102 (2016).
66. Kapeli, K. *et al.* Distinct and shared functions of ALS-associated proteins TDP-43, FUS and TAF15 revealed by multisystem analyses. *Nat Commun* **7**, 12143 (2016).
67. Kreiter, N. *et al.* Age-dependent neurodegeneration and organelle transport deficiencies in mutant TDP43 patient-derived neurons are independent of TDP43 aggregation. *Neurobiol Dis* **115**, 167–181 (2018).
68. Bilican, B. *et al.* Mutant induced pluripotent stem cell lines recapitulate aspects of TDP-43 proteinopathies and reveal cell-specific vulnerability. *Proc Natl Acad Sci U S A* **109**, 5803–8 (2012).
69. Kilpinen, H. *et al.* Common genetic variation drives molecular heterogeneity in human iPSCs. *Nature* **546**, 370–375 (2017).
70. Borthwick, G. M., Johnson, M. A., Ince, P. G., Shaw, P. J. & Turnbull, D. M. Mitochondrial enzyme activity in amyotrophic lateral sclerosis: implications for the role of mitochondria in neuronal cell death. *Ann Neurol* **46**, 787–90 (1999).
71. Wiedemann, F. R., Manfredi, G., Mawrin, C., Beal, M. F. & Schon, E. A. Mitochondrial DNA and respiratory chain function in spinal cords of ALS patients. *J Neurochem* **80**, 616–25 (2002).
72. Hor, J. H. *et al.* ALS motor neurons exhibit hallmark metabolic defects that are rescued by SIRT3 activation. *Cell Death Differ* **28**, 1379–1397 (2021).
73. Vandoorne, T. *et al.* Differentiation but not ALS mutations in FUS rewires motor neuron metabolism. *Nat Commun* **10**, (2019).
74. Devoy, A. *et al.* Humanized mutant FUS drives progressive motor neuron degeneration without aggregation in 'FUSDelta14' knockin mice. *Brain* **140**, 2797–2805 (2017).
75. Steg, L. C. *et al.* Novel epigenetic clock for fetal brain development predicts prenatal age for cellular stem cell models and derived neurons. *Mol Brain* **14**, 1–11 (2021).
76. Reber, S. *et al.* The phase separation-dependent FUS interactome reveals nuclear and cytoplasmic function of liquid-liquid phase separation. *Nucleic Acids Res* **49**, 7713–7731 (2021).

77. Hikiami, R. *et al.* Conformational change of RNA-helicase DHX30 by ALS/FTD-linked FUS induces mitochondrial dysfunction and cytosolic aggregates. *Sci Rep* **12**, 16030 (2022).
78. Wang, W. *et al.* The ALS disease-associated mutant TDP-43 impairs mitochondrial dynamics and function in motor neurons. *Hum Mol Genet* **22**, 4706–19 (2013).
79. Davis, S. A. *et al.* TDP-43 interacts with mitochondrial proteins critical for mitophagy and mitochondrial dynamics. *Neurosci Lett* **678**, 8–15 (2018).
80. Merkwirth, C. *et al.* Loss of prohibitin membrane scaffolds impairs mitochondrial architecture and leads to tau hyperphosphorylation and neurodegeneration. *PLoS Genet* **8**, e1003021 (2012).
81. Wei, Y., Chiang, W. C., Sumpter, R., Mishra, P. & Levine, B. Prohibitin 2 Is an Inner Mitochondrial Membrane Mitophagy Receptor. *Cell* **168**, 224-238.e10 (2017).
82. Naumann, M. *et al.* Impaired DNA damage response signaling by FUS-NLS mutations leads to neurodegeneration and FUS aggregate formation. *Nat Commun* **9**, 335 (2018).
83. Lenzken, S. C. *et al.* FUS-dependent phase separation initiates double-strand break repair. *BioRxiv* doi: 10.1101/798884 (2019) doi:10.1101/798884.
84. Wang, W.-Y. *et al.* Interaction of FUS and HDAC1 regulates DNA damage response and repair in neurons. *Nat Neurosci* **16**, 1383–91 (2013).
85. Stoccoro, A. *et al.* Mitochondrial DNA copy number and D-loop region methylation in carriers of amyotrophic lateral sclerosis gene mutations. *Epigenomics* **10**, 1431–1443 (2018).
86. Murakami, T. *et al.* ALS/FTD Mutation-Induced Phase Transition of FUS Liquid Droplets and Reversible Hydrogels into Irreversible Hydrogels Impairs RNP Granule Function. *Neuron* **88**, 678–690 (2015).
87. Yoshimura, A. *et al.* Myosin-Va Facilitates the Accumulation of mRNA/Protein Complex in Dendritic Spines. *Current Biology* **16**, 2345–2351 (2006).
88. Kanai, Y., Dohmae, N. & Hirokawa, N. Kinesin Transports RNA: Isolation and Characterization of an RNA-Transporting Granule. *Neuron* **43**, 513–525 (2004).
89. Hoell, J. I. *et al.* RNA targets of wild-type and mutant FET family proteins. *Nat Struct Mol Biol* **18**, 1428–31 (2011).
90. Oberstadt, M., Claßen, J., Arendt, T. & Holzer, M. TDP-43 and Cytoskeletal Proteins in ALS. *Mol Neurobiol* **55**, 3143–3151 (2018).
91. Fumagalli, L. *et al.* C9orf72-derived arginine-containing dipeptide repeats associate with axonal transport machinery and impede microtubule-based motility. *Sci Adv* **7**, (2021).
92. Sheng, Z. H. The Interplay of Axonal Energy Homeostasis and Mitochondrial Trafficking and Anchoring. *Trends Cell Biol* **27**, 403–416 (2017).
93. Chamberlain, K. A. & Sheng, Z.-H. Mechanisms for the maintenance and regulation of axonal energy supply. *J Neurosci Res* **97**, 897–913 (2019).
94. Attwell, D. & Laughlin, S. B. An energy budget for signaling in the grey matter of the brain. *J Cereb Blood Flow Metab* **21**, 1133–45 (2001).
95. Hallermann, S., de Kock, C. P. J., Stuart, G. J. & Kole, M. H. P. State and location dependence of action potential metabolic cost in cortical pyramidal neurons. *Nat Neurosci* **15**, 1007–14 (2012).
96. Lennie, P. The cost of cortical computation. *Current Biology* **13**, 493–497 (2003).

97. Harris, J. J. & Attwell, D. The energetics of CNS white matter. *J Neurosci* **32**, 356–71 (2012).
98. Verstreken, P. *et al.* Synaptic mitochondria are critical for mobilization of reserve pool vesicles at Drosophila neuromuscular junctions. *Neuron* **47**, 365–378 (2005).
99. Ma, H., Cai, Q., Lu, W., Sheng, Z.-H. & Mochida, S. KIF5B motor adaptor syntabulin maintains synaptic transmission in sympathetic neurons. *J Neurosci* **29**, 13019–29 (2009).
100. Ivannikov, M. V., Sugimori, M. & Llinás, R. R. Synaptic vesicle exocytosis in hippocampal synaptosomes correlates directly with total mitochondrial volume. *Journal of Molecular Neuroscience* **49**, 223–230 (2013).
101. Gautam, M. *et al.* SBT-272 improves TDP-43 pathology in ALS upper motor neurons by modulating mitochondrial integrity, motility, and function. *Neurobiol Dis* **178**, 106022 (2023).
102. Lee, Y. *et al.* Oligodendroglia metabolically support axons and contribute to neurodegeneration. *Nature* **487**, 443–8 (2012).
103. Joseph Bloom, A. *et al.* Disruption of lactate metabolism in the peripheral nervous system leads to motor-selective deficits. *BioRxiv* doi: 10.1101/2022.06.29.497865 (2022) doi:10.1101/2022.06.29.497865.
104. Patel, A. *et al.* Biochemistry: ATP as a biological hydrotrope. *Science (1979)* **356**, 753–756 (2017).
105. Raczynska, K. D. *et al.* FUS/TLS contributes to replication-dependent histone gene expression by interaction with U7 snRNPs and histone-specific transcription factors. *Nucleic Acids Res* **43**, 9711–28 (2015).
106. Flemr, M. & Bühler, M. Single-step generation of conditional knockout mouse embryonic stem cells. *Cell Rep* **12**, 709–716 (2015).
107. Yu, J. *et al.* Human induced pluripotent stem cells free of vector and transgene sequences. *Science* **324**, 797–801 (2009).
108. Schweingruber, C., Nijssen, J., Benitez, J. A. & Hedlund, E. Single-Cell mRNA-Seq of In Vitro-Derived Human Neurons Using Smart-Seq2. *Methods Mol Biol* **2594**, 143–164 (2023).
109. Picelli, S. *et al.* Full-length RNA-seq from single cells using Smart-seq2. *Nat Protoc* **9**, 171–81 (2014).
110. Dobin, A. *et al.* STAR: ultrafast universal RNA-seq aligner. *Bioinformatics* **29**, 15–21 (2013).
111. Ramsköld, D., Wang, E. T., Burge, C. B. & Sandberg, R. An abundance of ubiquitously expressed genes revealed by tissue transcriptome sequence data. *PLoS Comput Biol* **5**, 1–11 (2009).
112. R Core Team. R: A Language and Environment for Statistical Computing. Preprint at https://www.r-project.org/ (2021).
113. Love, M. I., Huber, W. & Anders, S. Moderated estimation of fold change and dispersion for RNA-seq data with DESeq2. *Genome Biol* **15**, 550 (2014).
114. Butler, A., Hoffman, P., Smibert, P., Papalexi, E. & Satija, R. Integrating single-cell transcriptomic data across different conditions, technologies, and species. *Nat Biotechnol* **36**, 411–420 (2018).
115. Divakaruni, A. S. & Jastroch, M. A practical guide for the analysis, standardization and interpretation of oxygen consumption measurements. *Nat Metab* **4**, 978–994 (2022).

116. Keuper, M. *et al.* Spare mitochondrial respiratory capacity permits human adipocytes to maintain ATP homeostasis under hypoglycemic conditions. *FASEB J* **28**, 761–70 (2014).
117. Schindelin, J. *et al.* Fiji: An open-source platform for biological-image analysis. *Nat Methods* **9**, 676–682 (2012).

Acknowledgements

FACS was performed at the Biomedicum Flow Cytometry core facility at the Karolinska Institutet. We thank the operators Linda Pannagel and Juan Basil for their assistance. The authors acknowledge support from the National Genomics Infrastructure in Stockholm funded by Science for Life Laboratory, the Knut and Alice Wallenberg Foundation and the Swedish Research Council, and SNIC/Uppsala Multidisciplinary Center for Advanced Computational Science for assistance with massively parallel sequencing and access to the UPPMAX computational infrastructure. We thank the NGI project coordinators Mattias Ormestad and Elísabet Einarsdóttir. Microscopy was performed at the Biomedicum Imaging Core (BIC) at the Karolinska Institutet and at the Imaging Facility at Stockholm University (IFSU). We thank the facility manager Chris Molenaar for his assistance. We thank all our group members for helpful discussions throughout the project.

This research was funded by the support from the Swedish Research Council (2020-01049), Radala Foundation, Ulla-Carin Lindquist's foundation for ALS research, Åhlen-stiftelsen (Åhlen's Foundation, grant numbers 223060, 213051, 203030, and 193042), and the Swedish Brain Foundation (Hjärnfonden, grant number FO2021-0145) to E.H. C.S. was supported by an early post.doc mobility fellowship by the Swiss National Science Foundation (grant number 172233). J.A.B. was supported by a postdoctoral fellowship from the Swedish Society for Medical Research (SSMF). This research was also supported by the NOMIS Foundation, the UK Dementia Research Institute (grant number UK DRI-6005) which receives its funding from UK DRI Ltd, funded by the UK Medical Research Council, Alzheimer's Society and Alzheimer's Research UK, the Medical Research Council (grant number MR/S025898/1), the John and Lucille van Geest foundation, and the Motor Neurone Disease Association (grant number 872-791) to M.-D.R. M.K. and M.J. are supported by the Novo Nordisk Foundation (grant number 0059646).

Author contributions

E.H., M.-D.R.: conceptualization of study, supervision and project administration. E.H., M.-D.R., M.J.: funding acquisition. E.H., M.-D.R.: supervision. E.H., M.-D.R., C.S., J.N., J.A.B., S.R.: methodology and study design. S.R., C.S.: literature review and meta-analysis of clinical features. S.R., J.M., N.O'B., J.A.B., M.-D.R.: genome editing and characterization of iPSC lines. C.S., J.N., J.A.B.: experimental work on neuronal culture and single-cell sorting. C.S., J.A.B.: single cell library preparation. C.S., MK: experimental work on metabolic assays (Seahorse). M.K.: metabolic analysis. C.S.: experimental work and analysis of mitochondrial motility. J.N., I.M.: RNA-sequencing data processing, differential gene expression analysis, and gene set enrichment analysis. J.N., J.M., C.S.: Ingenuity pathway analysis. J.N., C.S.: preparation of figures. C.S., E.H.: writing of original draft. All authors contributed to editing of the article and approved the manuscript.

Abbreviations

ALS	amyotrophic lateral sclerosis
ANOVA	analysis of variance
ATP	adenosine triphosphate
2-DG	2-deoxyglucose
CCA	canonical correlation analysis
DEA	differential (gene) expression analysis
DEG	differentially expressed genes
DNP	2,4-dinitrophenol
DTT	dithiothreitol
ECAR	extracellular acidification rate
FDR	false discovery rate
GO	gene ontology
GOF	gain of function
GSEA	gene set enrichment analysis
HRE	hexanucleotide repeat expansion (in C9orf72)
IPA	Ingenuity pathway analysis
iPSC	induced pluripotent stem cells
KO	knockout
LOF	loss of function
OCR	oxygen consumption rate
PCR	polymerase chain reaction
RPKM	reads per kilobase of exon per million reads mapped
SEM	standard error of the mean
UMAP	uniform manifold approximation and projection

Figures

Figure 1

Schweingruber et al., 2023

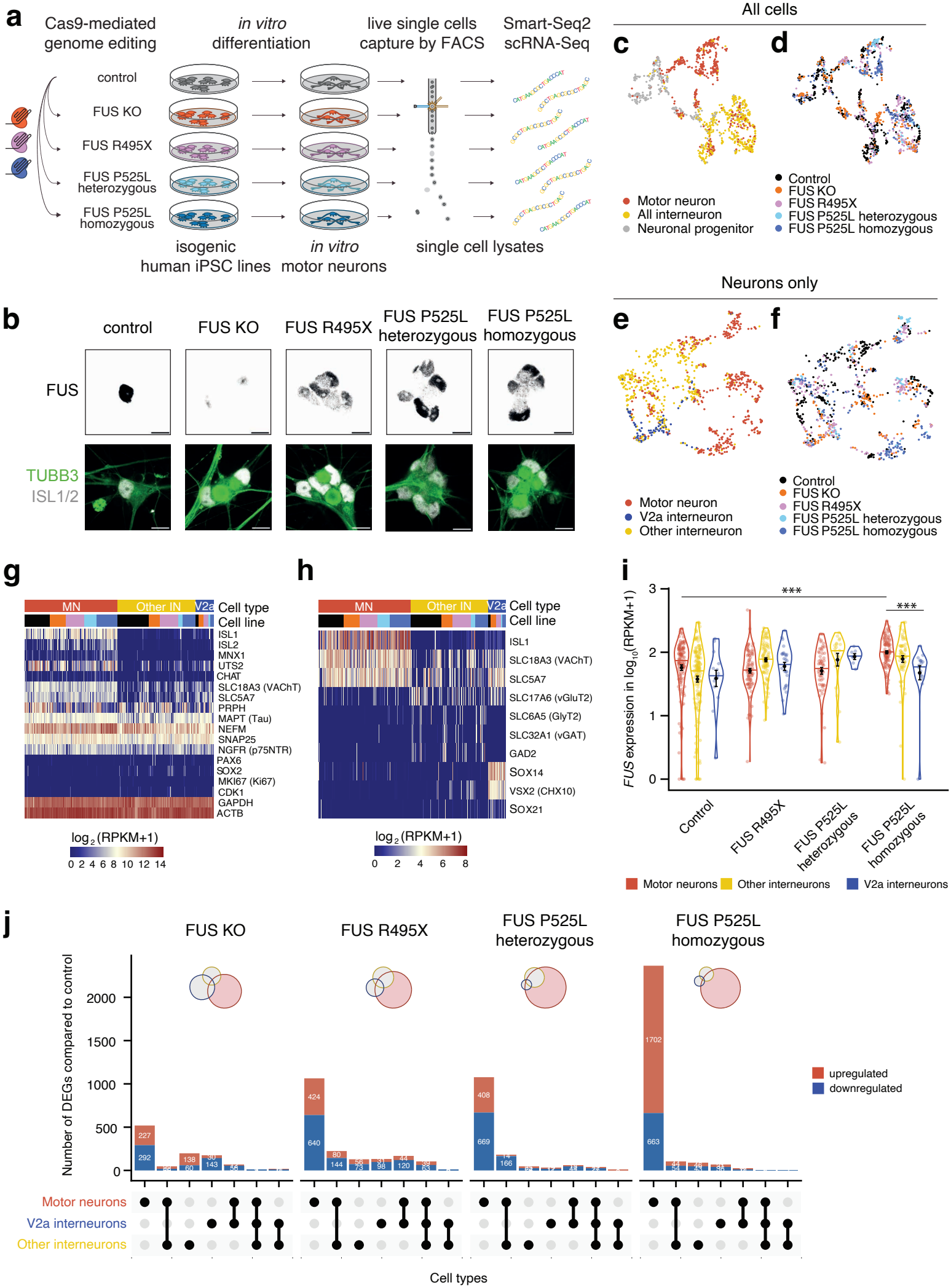

Figure 1. Single-cell RNA-Sequencing identifies RNA dysregulation specific to motor neurons with *FUS* mutations in a dose-dependent manner. a, Schematic showing generation of the different iPSC-lines using CRISPR-Cas9 gene editing, subsequent differentiation into motor neurons and interneurons, sorting and single-cell RNA sequencing. **b,** Confocal fluorescence microscopy with immunostaining of N-terminal FUS in motor neurons (TUBB3+, ISL1/2+) at day 28 reveals cytoplasmic accumulation of FUS R495X as well as P525L and ablation in the FUS KO line. Scale bars are 10 µm. **c**-**f**, UMAP projections of all cells of the included cell lines that passed quality control. The top two UMAPs are colored by assigned **c**, cell type or **d**, cell line, the bottom two only contain all neuronal cells, again colored by assigned **e**, cell type or **f**, cell line. **g**, Gene expression heatmaps of all neuronal cells, showing expression data of several (motor-)neuronal marker genes, progenitor markers and housekeeping genes. **h**, Gene expression heatmaps of specific motor- and interneuron subtype marker genes. **i,** Violin plots of the *FUS* mRNA expression in the control and ALS mutant lines across cell types. The normalized expression is given as RPKM. Differential expression was performed within cell type, across lines. Error bars show mean ± standard error of the mean (SEM). * $p<0.05$, ** $p<0.01$, *** $p<0.001$, derived from DEA using DESeq2. **j**, Upset plots showing the overlap between DEGs in motor neurons, V2a interneurons and other interneurons between the *FUS* mutant lines versus the control cell line. Each column represents a section of a Venn diagram of the cell types as indicated in the table below. The corresponding Venn diagram is shown in an insert. The red (top) and blue (bottom) columns represent upregulated and downregulated genes, respectively. Genes with an adjusted p-value of < 0.05 were considered differentially expressed.

Figure 2

Schweingruber et al., 2023

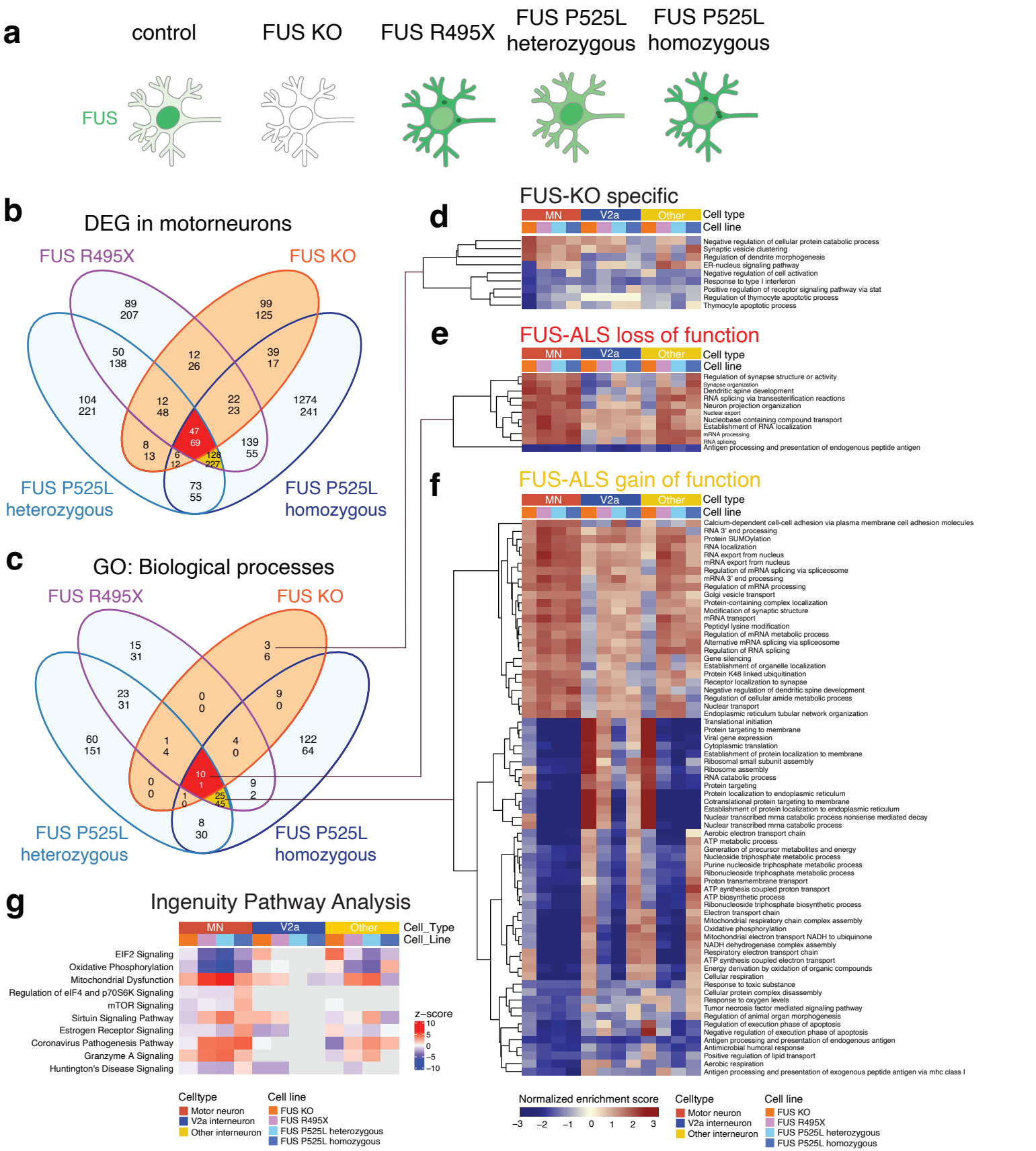

Figure 2. Shared dysregulated pathways in motor neurons across FUS mutations link mainly to gain-of-function. a, Schematics with representative patterns of different nuclear and cytoplasmic FUS protein localization in the cell lines used in this study. **b**, Venn diagram showing overlap between DEGs in the different FUS mutant and control motor neurons. Genes with an adjusted p-value of < 0.05 were considered differentially expressed. GO (biological process) pathways enriched or depleted in the different FUS mutant compared to the control motor neurons (using GSEA). For **b-c**, in each Venn compartment, the top number represents upregulated genes/processes, while the bottom number represents downregulated genes/processes. Pathways with an adjusted p-value of < 0.05 were considered significantly up- or downregulated. **d-f**, Heatmaps display the normalized enrichment scores (from GSEA) of selected groups of pathways from the Venn diagram in **c**. Motor neurons are compared to V2a or other interneurons to show specific or stronger regulation of these pathways in motor neurons. **g**, Top dysregulated pathways across FUS mutant motor neurons using the Ingenuity Pathways Analysis.

Figure 3

Schweingruber et al., 2023

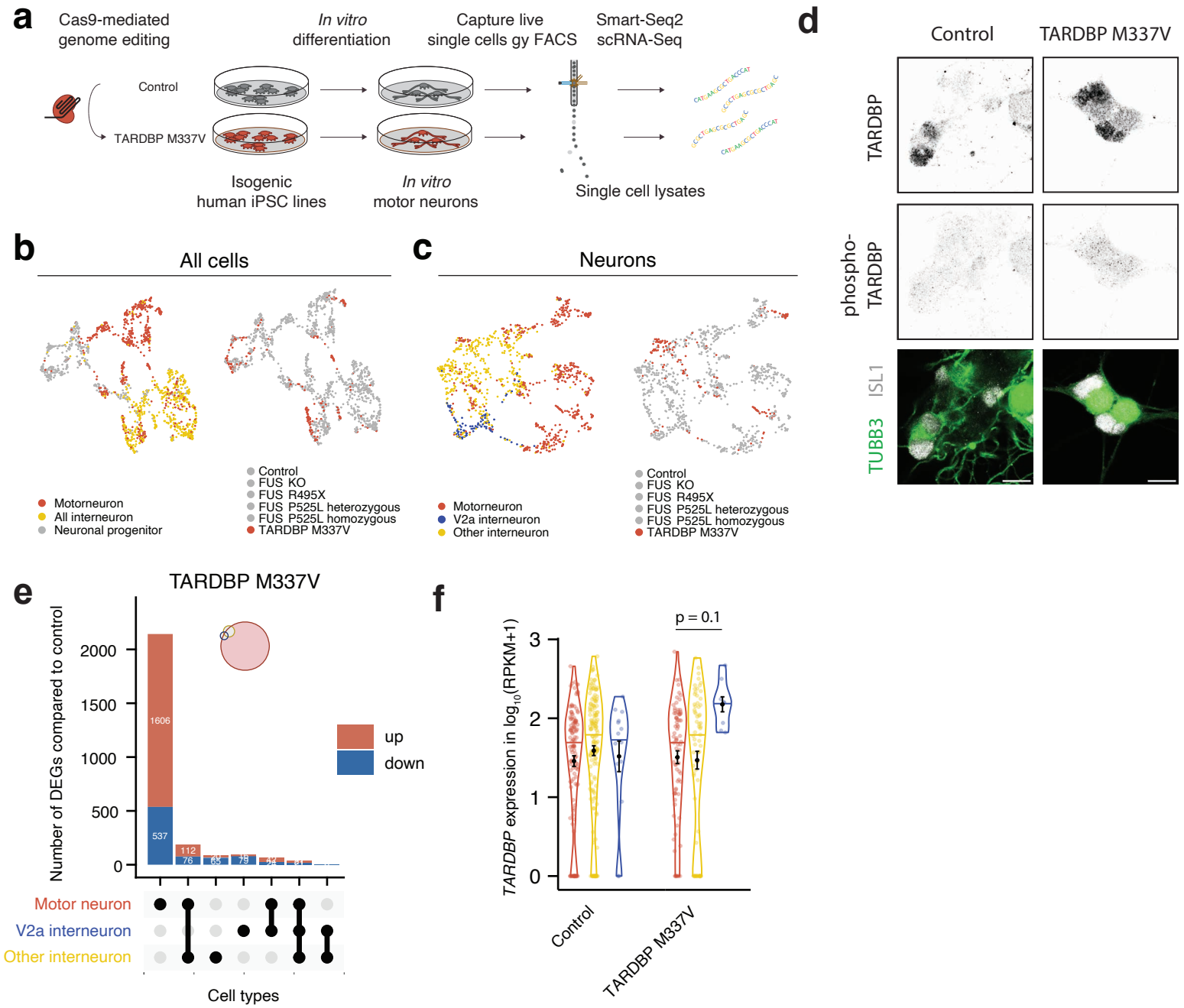

Figure 3. TARDBP M337V result in transcriptomic dysregulation unique to motor neurons.
a, Schematic of the generation of the TDP-43 M337V mutant iPSC line, differentiation into motor neurons and subsequent single-cell sorting and RNA-sequencing. **b**, UMAP projections of all single cells in the study that passed quality control. The two UMAPs are colored by assigned cell type (left) or cell line (right). **c**, UMAP projections of all neuronal cells in the study that passed quality control, again colored by assigned cell type (left) or cell line (right). **d,** TARDBP M337V is mainly nuclear but also forms phosphorylated cytoplasmic foci in motor neurons. Confocal fluorescence microscopy with immunostaining of antibodies against TARDBP and phosphor-TARDBP (S409/S410) in motor neurons (TUBB3+, ISL1/2+) at day 28. Scale bars are 10 µm. **e,** Violin plots of the *TARDBP* mRNA expression in the control and TARDBP M337V lines across cell types. The normalized expression is given as RPKM. Differential expression was performed within cell type, across lines. Error bars show mean ± SEM, * $p<0.05$, ** $p<0.01$, *** $p<0.001$, derived from DEA using DESeq2. **f**, Upset plots showing the overlap between DEGs in motor neurons, V2a interneurons and other interneurons between the *FUS* mutant lines versus the control cell line. Each column represents a section of a Venn diagram of the cell types as indicated in the table below. The corresponding Venn diagram is shown in an insert. The red top and blue bottom column represents upregulated and downregulated genes, respectively. Genes with an adjusted p-value of < 0.05 were considered differentially expressed.

Figure 4

Schweingruber et al., 2023

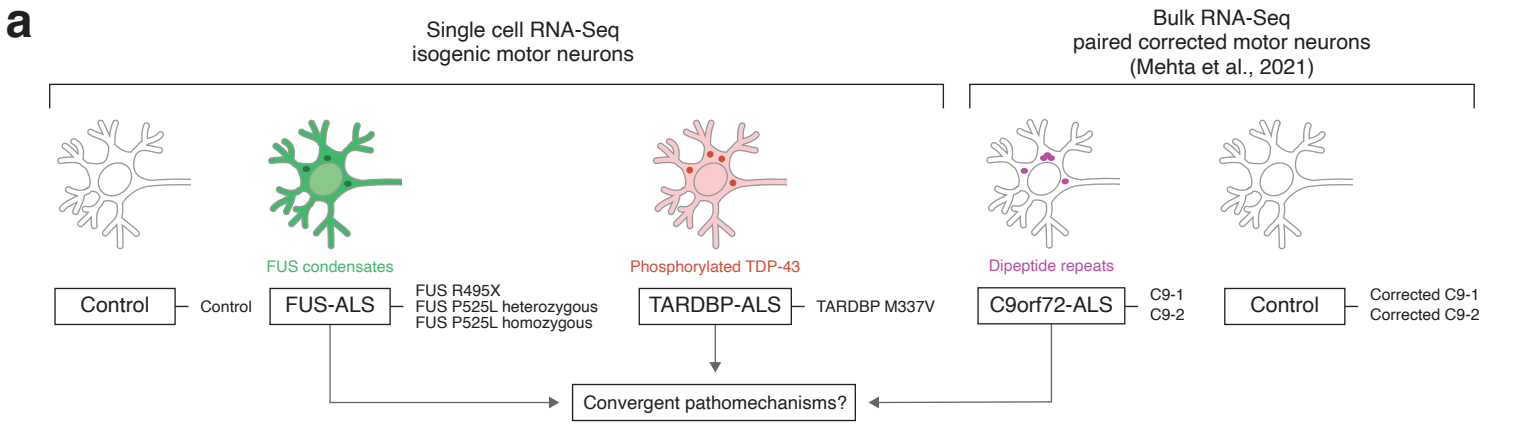

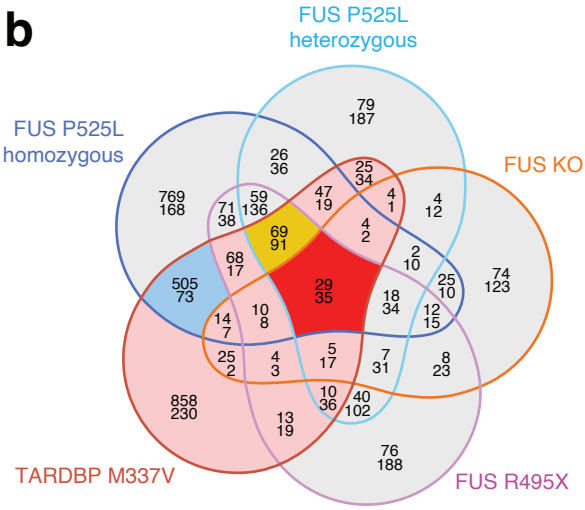

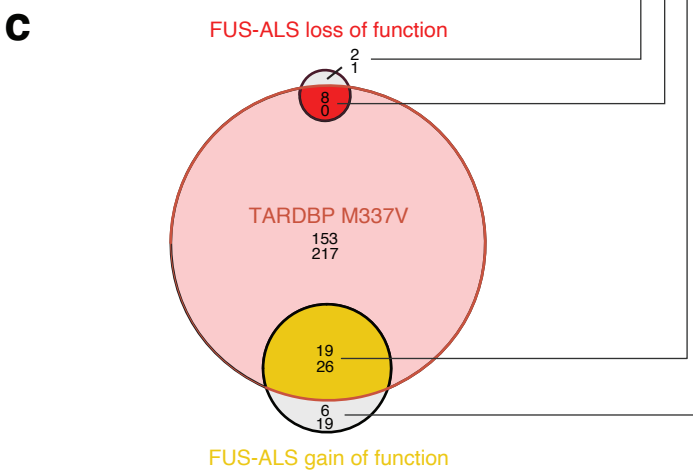

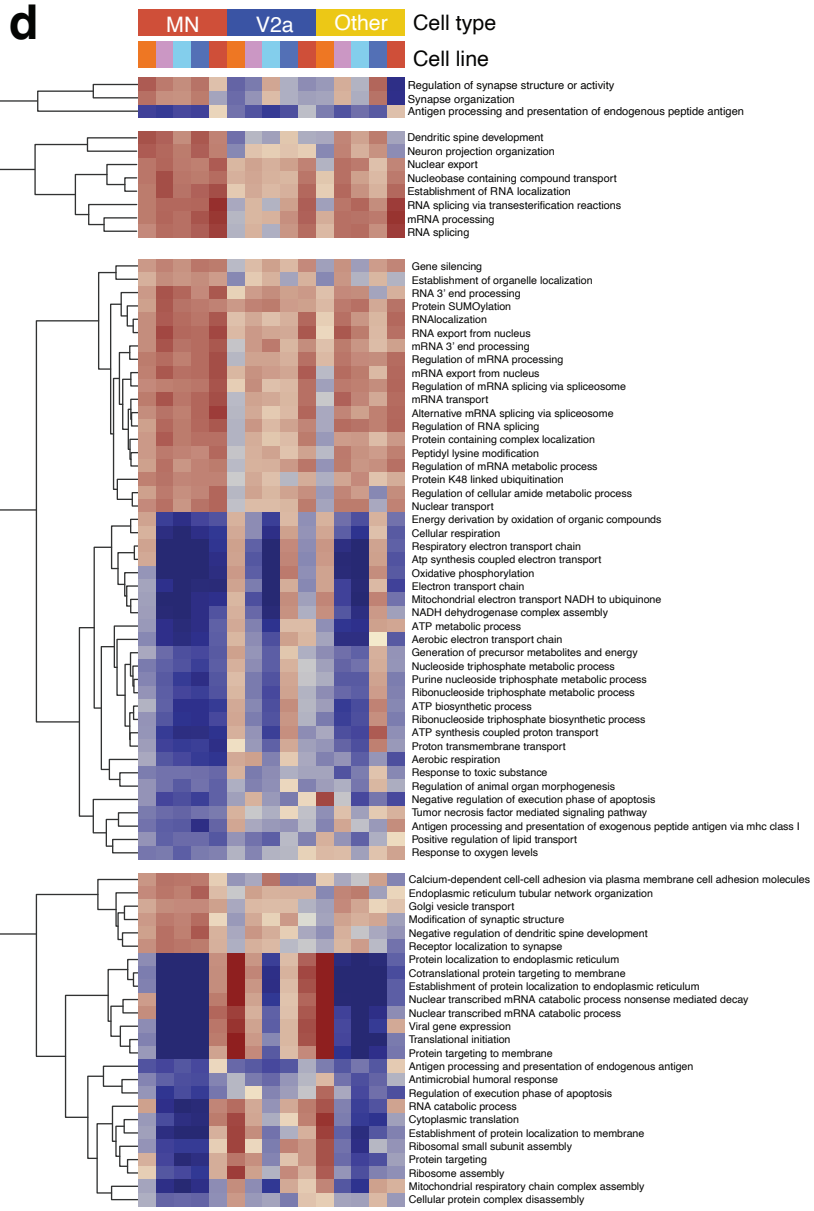

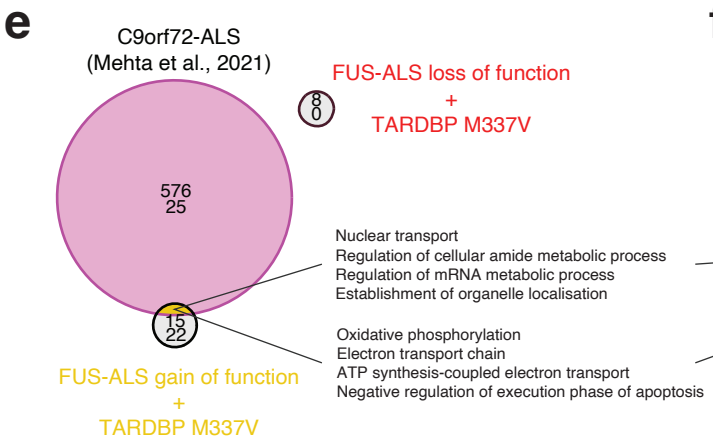

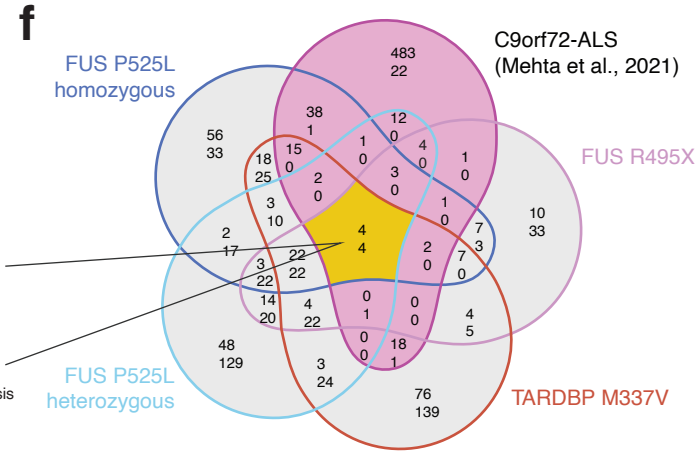

Figure 4. Cross-comparisons among FUS-, TARDBP-, and *C9orf72*-ALS reveal shared dysfunctions that converge on metabolic pathways. a, Strategy to uncover shared dysfunction across familial ALS forms that could uncover convergent pathomechanisms that are intrinsic to motor neurons. Cross-comparison of *FUS*-ALS and *TARDBP*-ALS motor neurons across our single-cell RNA-Seq data set (**b-d**) followed by cross-comparison with external bulk RNA-Seq dataset from *C9orf72*-ALS[33] was thus conducted (**e,f**). **b**, Venn diagram showing overlap of DEGs between all FUS mutant motor neurons, as well as the TARDBP mutant motor neurons, as compared to control. Genes with an adjusted p-value of < 0.05 were considered differentially expressed. **c**, Venn diagram showing overlap in dysregulated biological processes between FUS LOF lines (all FUS lines), FUS GOF lines (excluding the FUS KO), and the TDP-43 M337V line following GSEA. For **b-c**, in each compartment, the top number represents upregulated genes/pathways, while the bottom number represents downregulated genes/pathways. Pathways with an adjusted p-value of < 0.05 were considered significantly up- or downregulated. **d**, Heatmaps displaying normalized enrichment scores from GSEA of selected groups of pathways from the Venn diagram in **c**. Motor neurons are compared to V2a interneurons to show specific or stronger regulation of these pathways in motor neurons. **e**, Venn diagram depicting the overlap between dysregulated biological processes in TARDBP M337V and the ALS-FUS GOF and LOF groups defined in fig. 3. **f,** Venn diagram depicting the overlap between dysregulated pathways from the single cells RNA-Seq of ALS mutant motor neurons (FUS R495X, FUS P525L lines and TARDBP M337V) and the bulk RNA-Seq of *C9orf72*-ALS motor neurons.

Figure 5

Schweingruber et al., 2023

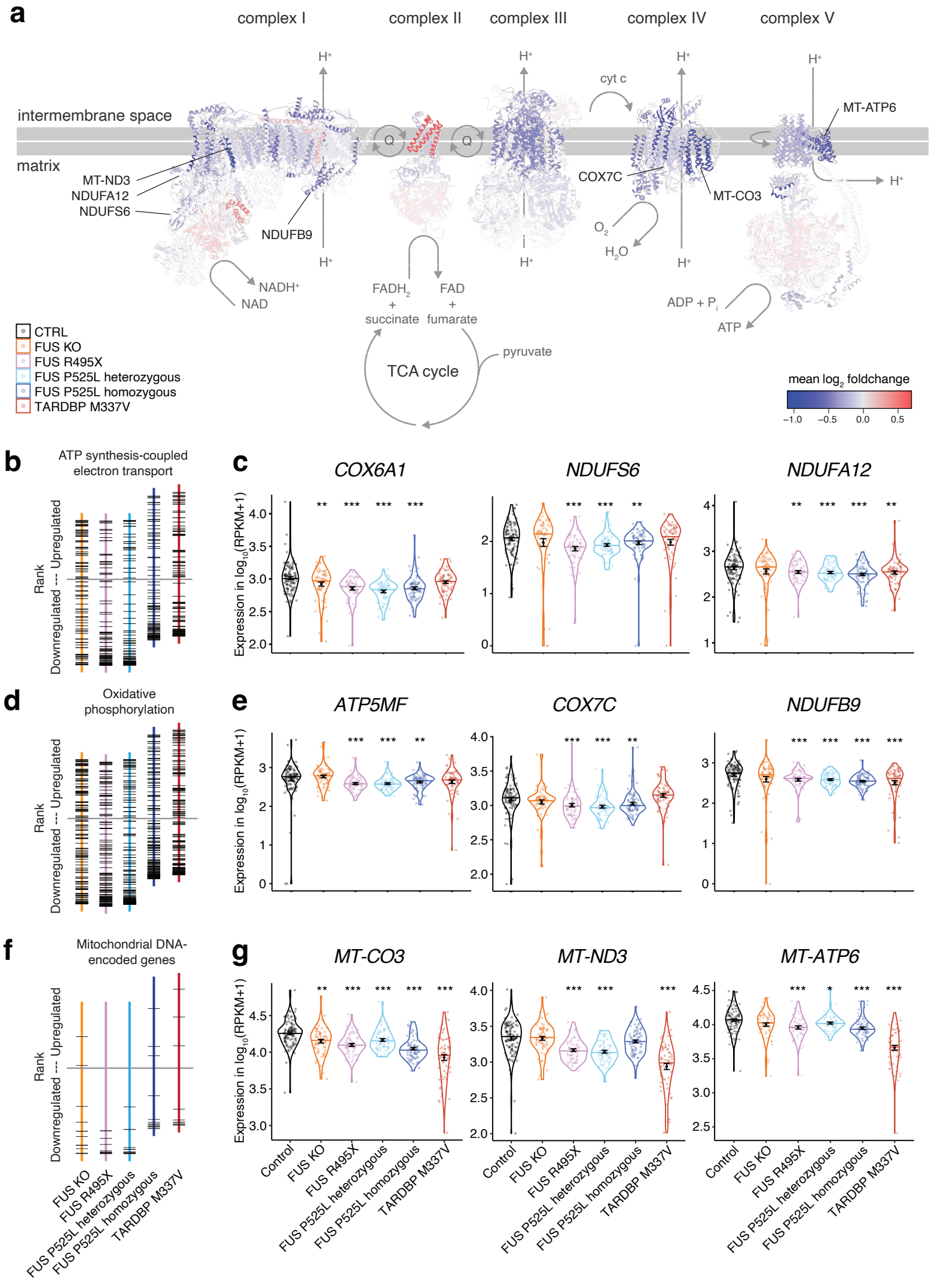

Figure 5. Dysregulation in key mitochondrial genes and pathways points to metabolic impairment in motor neurons across isogenic ALS lines. a, The mean expression change of respiratory genes in ALS motor neurons (as mean $\log_2$ foldchange of FUS R495X, FUS P525L heterozygous, FUS P525L homozygous, and TDP-43 M337V compared to control) was mapped to the protein structures of the mammalian mitochondrial respiratory complexes I–V (PDB entries 5lc5, 1zoy, 1bgy, 1occ, and 5ara) and rendered in UCSF Chimera. The composition was inspired by Sousa et al., 2018. The location of genes from expression plots in **c,e,g** are indicated with pointers. **b,d,f,** Modified GSEA plots showing the rank of all genes within this specific GO-term for all mutant motor neurons generated using the homogeneous protocol, according to the GSEA test statistic. The most significantly upregulated gene is on the top and the most significantly downregulated gene on the bottom. **c**,**e,g,** Violin plots showing normalized expression values (RPKM) of three example genes of the pathway from **b,d,f** in motor neurons generated with the homogeneous protocol. Error bars show mean ± SEM. * $p < 0.05$, ** $p < 0.01$, *** $p < 0.001$ vs. control, derived from DESeq2 differential gene expression.

Figure 6

Schweingruber et al., 2023

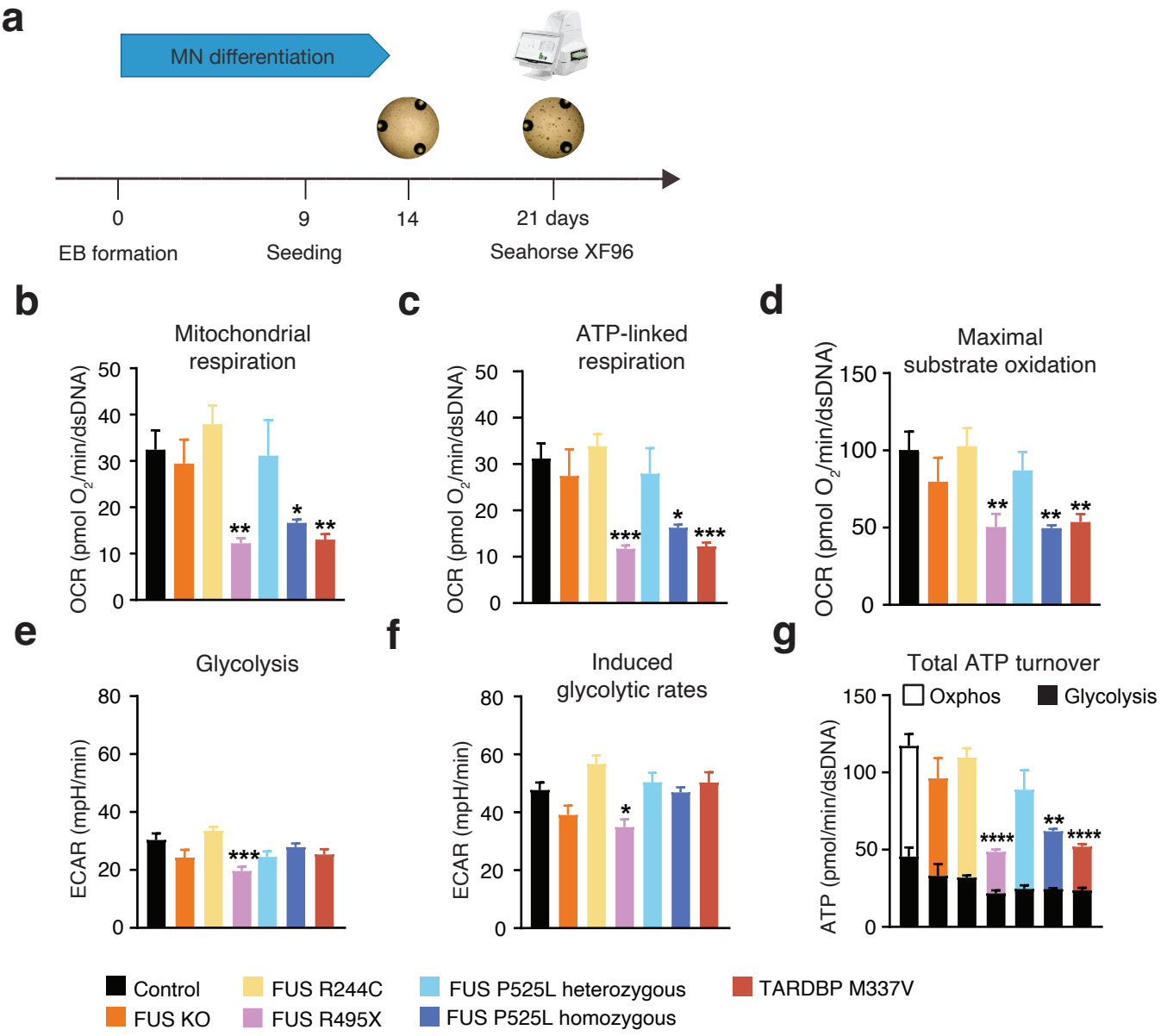

Figure 6. ***FUS*-ALS and *TARDBP*-ALS motor neurons showed impaired bioenergetics linked to protein mis-localization. a**, Scheme depicting time-course of the metabolic assay. Following differentiation with the homogenous protocol, motor neurons were assessed at day 21 using a XF96 extracellular flux analyzer to measure oxygen consumption rates (OCR) and extracellular acidification rates (ECAR). Aggregated OCR and ECAR traces and their dissection into functional modules are shown in Extended Data Fig. 6. **b**, Mitochondrial respiration, **c**, ATP-linked respiration after subtracting proton leak respiration (Extended Data Fig. 6g), **d**, Maximal substrate oxidation upon addition of uncoupler DNP, 100 µM, **e**, glycolytic ECAR at baseline and **f**, induced glycolysis after inhibition of mitochondrial ATP synthase; **f,** Calculation of cellular ATP turnover from glycolysis and oxidative phosphorylation. Glycolytic proton production rates were converted to glycolytic ATP output assuming a P/H^+ ratio of 1:1 (black part of bars) and ATP-linked OCR was converted to mitochondrial ATP output assuming a P/O ratio of 2.3 (top part of bars). Data are the mean + SEM of 16-19 wells measured for three independent differentiations. * $p<0.05$, ** $p<0.01$, *** $p<0.001$, **** $p< 0.0001$ vs. control, One-way ANOVA (posthoc: Dunnett's).

Figure 7

Schweingruber et al., 2023

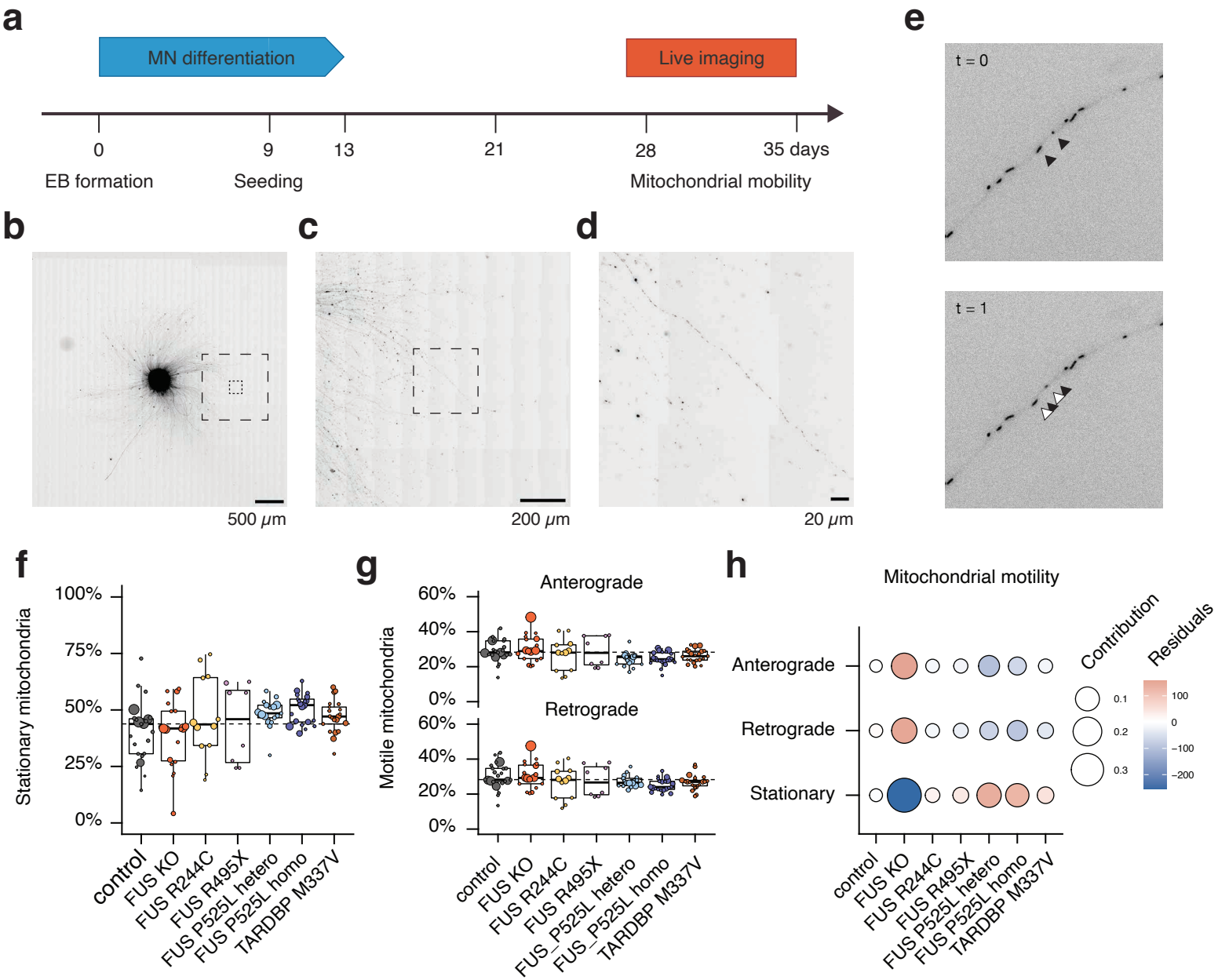

Figure 7. ALS motor axons show dysfunction in mitochondrial motility. a, Schematic of the mitochondrial motility assays using live fluorescence microscopy. Motor neuron progenitors were attached as neurospheres, followed by terminal differentiation and axon outgrowth. Mitochondria were labeled using TMRM. **b-d**, Individual mitochondria become discernable at increasing magnifications (**b**, **c**), and were recorded in peripheral axons **d**. Scale bars are as indicated, ranging from 500 µm down to 20 µm. **e,** 6-min long timelapses were recorded at 0.5 Hz in 3-4 locations in at least 3 independent differentiations per line. **f-h**, Traces were identified using TrackMate 7 with StarDist detector and simple LAP tracer and directional movement was analyzed in R using our package 'mitotrackR'. The proportions of stationary (**f**) and motile mitochondria (**g**) were calculated. Each bubble represents the number of mitochondria in individual recordings. **h**, The influence of the mutation in isogenic motor neurons on the mitochondrial motility (as proporation of stationary, anterograde and retrograde mobile mitochondria) was assessed by Pearson's χ^2 test ($\chi^2 = 88192$, df = 12, $p < 2.2e-16$). The association between isogenic mutants and mitochondrial motility is plotted. The sign of the residuals indicates the direction of the association, with attraction and repulsion colored as red and blue, respectively. The bubble size represents the contribution to the total χ^2 score (squared residuals over χ^2 statistic).